The University of Maine
DigitalCommons@UMaine

Electronic Theses and Dissertations | Fogler Library

Fall 5-3-2024

Development of a Clay Characterization Procedure Using Atterberg Limits for Additive Manufacturing

Rakesh K. Pandit
University of Maine, rakesh.k.pandit@maine.edu

Follow this and additional works at: https://digitalcommons.library.umaine.edu/etd

 Part of the Geotechnical Engineering Commons

Recommended Citation

Pandit, Rakesh K., "Development of a Clay Characterization Procedure Using Atterberg Limits for Additive Manufacturing" (2024). *Electronic Theses and Dissertations*. 3973.
https://digitalcommons.library.umaine.edu/etd/3973

This Open-Access Thesis is brought to you for free and open access by DigitalCommons@UMaine. It has been accepted for inclusion in Electronic Theses and Dissertations by an authorized administrator of DigitalCommons@UMaine. For more information, please contact um.library.technical.services@maine.edu.

DEVELOPMENT OF A CLAY CHARACTERIZATION PROCEDURE USING ATTERBERG LIMITS FOR ADDITIVE MANUFACTURING

By

Rakesh Kumar Pandit

B.E. Tribhuvan University, Nepal, 2021

A THESIS

Submitted in Partial Fulfillment of the

Requirements for the Degree of

Master of Science

(in Civil Engineering)

The Graduate School

The University of Maine

May 2024

Advisory Committee:

Prof. Luis Zambrano Cruzatty, Assistant Professor of Civil and Environmental Engineering, Advisor

Prof. Aaron Gallant, Associate Professor of Civil and Environmental Engineering

Prof. Roberto Lopez-Anido, Professor of Civil and Environmental Engineering

© 2024 By Name
All Rights Reserved

DEVELOPMENT OF A CLAY CHARACTERIZATION PROCEDURE USING ATTERBERG LIMITS FOR ADDITIVE MANUFACTURING

By Rakesh Kumar Pandit

Thesis Advisor: Dr. Luis Zambrano-Cruzatty

An Abstract of the Thesis Presented
in Partial Fulfillment of the Requirements for the
Degree of Master of Science
(in Civil Engineering)
May 2024

Recently, additive manufacturing (AM) using earthen materials (natural earth components such as clay, silt, and sand) has been proposed as a sustainable alternative to conventional concrete-based construction practices for its potential to reduce carbon footprint. Some research groups suggest zero-transportation construction can be achieved using local or “indigenous" soils. However, the heterogeneous nature of these soils can impose significant challenges associated with fine-tuning the soil mixture and the printing parameters for the extrusion, deposition, and curing process. Understanding the mechanical links between the extrusion process and the behavior of earthen materials is critical to developing the potential of AM using earthen materials. Among the components of earthen mixtures, the percent of clay plays a key role, providing cohesive binding and flexibility to the mixture required to pump and extrude the material. Thus, studying the isolated parameters of the clay is essential to developing the design of earthen mixtures that fulfill the stringent criteria that materials need for AM purposes.

This research elucidates the role of Atterberg limits and liquidity index in optimizing the extrudability and quality of 3D-printed clay objects. Three mathematical models are proposed to capture the role of the mentioned parameters in the extrusion process: first, one linking threshold pressure on the piston to initiate clay paste extrusion with liquidity

index and geometry of the tank; second, linking printing pressure with liquidity index, extrusion velocity, bead height and width, and geometry of the equipment parts involved in the printing process; and third, one for predicting post-drying shrinkage based on water content and Atterberg's limits. An extensive experimental program was conducted with three different types of clay (Kaolinite, Cibas, and Presumpscot), using a WASP 40100 clay 3D printer to validate the model. The findings indicate that the liquidity index significantly influences the extrusion pressure due to its correlation with the undrained shear strength of the clay. It was also found that a simple flow rate test can be used to determine the optimum printing pressure vs. liquidity index, to avoid under and over-extrusion of clay paste. It is also found that the optimum range of clay consistency is between a liquidity index of 50-80%, correlating to a defined pressure range of 250-850 kPa in the WASP 40100 clay printer. This research contributes valuable insights into the use of Atterberg limits and soil mechanics principles to characterize the use of clay in the AM process and opens research opportunities oriented to studying the behavior of soil mixtures for AM.

DEVELOPMENT OF A CLAY CHARACTERIZATION PROCEDURE USING ATTERBERG LIMITS FOR ADDITIVE MANUFACTURING

By Rakesh Kumar Pandit

Thesis Advisor: Dr. Luis Zambrano-Cruzatty

A Lay Abstract of the Thesis Presented
in Partial Fulfillment of the Requirements for the
Degree of Master of Science
(in Civil Engineering)
May 2024

Keywords: additive manufacturing, 3d printing, atterberg's limits, undrained shear strength, liquidity index, shrinkage

DEDICATION

To Lord Krishna, the Almighty, whose divine wisdom guides my every step, I dedicate this work in reverence and gratitude for the unending grace and inspiration bestowed upon me.

ACKNOWLEDGEMENTS

I would like to express my deepest appreciation to my advisor, Prof. Luis Zambrano-Cruzatty, whose expertise, understanding, and patience considerably enhanced my graduate experience. His guidance was the beacon that guided me through this academic journey, and his encouragement and support ignited my potential to bring this research to fruition.

I am indebted to Prof. Aaron Gallant, whose insights and feedback were invaluable in shaping this research. I would also like to thank Prof. Roberto Lopez-Anido for his valuable guidance.

My sincere thanks go to the faculty and friends at the University of Maine for a supportive environment. They were always there to listen and offer advice. My appreciation would be incomplete without acknowledging Molly Rathbun's support in performing the lab experiments.

Lastly, and most importantly, I wish to thank my family: my father, my mother, and my siblings, for their unconditional love, moral support, and constant encouragement throughout my life. They are my foundation, and I am truly grateful for everything they have done for me.

I know that these words of thanks are just a small token of appreciation compared to the endless support and patience they have all shown me.

TABLE OF CONTENTS

LIST OF TABLES

LIST OF FIGURES

CHAPTER 1

INTRODUCTION

Additive manufacturing (AM) or 3D printing is a process that creates a physical object by the adhesion of layers from a digital model [7]. Since its introduction, the realm of AM has evolved continuously, pushing the boundaries of creativity and functionality across various industries. It has emerged as a transformative technology, revolutionizing the way we design, prototype, and manufacture a wide range of products. Recent developments have reduced the cost of 3D printers, thereby expanding their applications in schools, homes, libraries, and laboratories. While the application of 3D printing has been extensively explored for various materials, such as plastics and metals, the use of earthen materials as a 3D printing feedstock has gained increasing attention in recent years [8]. In particular, liquid deposition modeling (LDM), a type of 3D printing mechanism for ceramics, which consists of depositing layers in a viscous fluid state at room temperature and subsequent solidification by evaporation of water or other solvents, has made possible the utilization of materials with the potential to revolutionize various sectors, including the construction sector [9, 10, 11, 12, 13]. AM stands at the intersection of technology and architecture, which has allowed the exploration of alternative and more sustainable construction materials that could partially replace concrete like earthen materials [5, 14, 15, 6].

Earthen construction presents a viable solution for building affordable housing in low-income countries, providing shelters in disaster-prone areas and for refugees [11]. By integrating 3D printing technology and utilizing locally sourced materials, construction time can be drastically reduced from years to mere months, leading to significant cost savings [11]. Since the shelters for refugees are intended to be temporary, leveraging such technology offers a practical alternative for optimizing construction expenditure while ensuring swift project completion.

Earthen materials with a high content of plastic clay are attractive choices for AM because they are naturally occurring and abundant on the Earth's surface. The clay when mixed with water has flowability and strong interparticle forces, which can be enhanced by densification or cementation. The clay is a cohesive soil and is considered the binder of the mixture. The ability to 3D print with clay opens up new avenues for the creation of intricate, bespoke architectural elements and building components. Unlike traditional construction methods, 3D clay printing allows for the fabrication of complex geometries, reduced material waste, and the potential for on-site or near-site production, thereby minimizing the environmental impact. According to recent research, nearly one-third of total greenhouse gas emissions are attributed to building construction [16, 17]. Alhumayani et al. [18] suggest that the utilization of 3D printing for earth-based materials could yield favorable environmental outcomes by decreasing carbon footprints, transportation, and construction waste. Mud constructions offer significant savings in heating during winter and cooling in summer due to their thermal inertia [15]. Additionally, clays' ability to absorb and evaporate moisture helps regulate humidity, promoting a healthier indoor climate [15]. 3D printing in earthen construction blends the ancient practice of using clay as a building material with the precision and speed of modern AM techniques, promising an attractive alternative in the low-rise construction industry.

Despite the numerous benefits of earthen materials and AM as an alternative to concrete and conventional construction methods, there are still barriers that could prevent their use. For example, the reliability of the technology, the lack of construction codes, negative social perceptions, and a knowledge gap about the material's durability, strength, and maintenance. Furthermore, there are processing challenges related to void formation which can reduce the mechanical performance due to a reduction in interfacial bonding between printed layers. The other challenges are anisotropic behavior, the limitation of computer-aided design, layer-by-layer appearance, and limited knowledge of how earthen materials will deform under gravitational loads drifting from the intended design [19].

The uncertain and heterogeneous nature of soils imposes a challenge in standardizing the strengths and workability of earthen materials. The successful integration of 3D clay printing into the construction industry requires a comprehensive understanding of the material's rheological behavior, the influence of formulation parameters, and the optimization of the printing process. Factors such as the clay composition, water content, and the design of the printing nozzle and extrusion system can significantly impact the printability, structural integrity, and overall performance of the final printed components. Because of this, studies that look at determining the controlling parameters of earthen materials during the extrusion and post-printing are highly desirable.

Clay's exceptional malleability facilitates significant adjustments before, during, and after the 3D printing process, rendering it particularly well-suited for explorations in this technology [20]. Material properties like moisture content, color, and texture of clay, along with tools (3D printer, extrusion type, extrusion nozzle, printing speed) and 3D printing settings including tool paths, are crucial variables with substantial impacts on shaping the outcome. Even with a simple digital model, by playing with the physical and material parameters of digital fabrication, it is possible to obtain many different outcomes most of which cannot be foreseen before materialization [20].

This study's objective is to elucidate the role of Atterberg limits as controlling properties for the design and optimization of the printing process. This work shows that the liquidity index is a controlling state parameter that helps fine-tune the extrudability, density, and quality of clay 3D-printed objects. Analytical models are developed that relate various parameters such as liquidity index (LI), undrained shear strength (S_u), extrusion rate, nozzle diameter, and bid thickness, to the extrusion pressure during 3D printing of clay-based materials. To verify those models, the experimental programs are conducted using three types of clay materials with varying Atterberg limits. Understanding the configuration of the printer, moisture, and properties of soil, helps to find out the pressure supply needed during printing either for research or industry. It also helps to manufacture

extrusion equipment efficiently as per the pressure requirement. Furthermore, an experimental procedure called the 'flow rate test' is explained to determine optimum printing pressure experimentally. And, a shrinkage prediction model is developed which predicts the shrinkage of specimens in advance based on the water content of clay. It helps to scale the size of the model so that the final specimen of the target size is obtained after drying. To fulfill the objective of the research, research questions are formulated which are presented in the following section. The subsequent sections after the research questions are the hypotheses made to proceed with the research to answer the research questions and the research objectives.

1.1 Research Questions

The following questions are answered by this thesis, which gives a great insight into the importance of considering LI of clay paste during 3D printing.

1. How are threshold and operating pneumatic pressures related to the moisture content/liquidity index of the soil?

2. How do threshold and operating pneumatic pressures change with the change in geometry of the extrusion equipment?

3. How is the shrinkage of the 3D-printed specimen from clay related to its moisture content during printing?

1.2 Hypotheses

In pursuit of refining additive manufacturing processes with clay, this thesis aims to establish a clay characterization procedure, specifically targeting Atterberg limits. The following hypotheses have been formulated as guiding principles in exploring and understanding the dynamics of clay paste extrusion.

1. LI and its effect on undrained shear strength are linkable with the printing pressure

   LI of the clay has a well-defined correlation with the S_u given by equation 1.1 developed by Wroth and Wood [21].

$$S_u = 170exp(-4.6LI) \tag{1.1}$$

   Equation 1.1 shows that S_u increases exponentially with a decrease in LI and decreases exponentially with an increase in LI. With the decrease in LI (or decrease in water content) of the clay, the cohesive force increases which increase S_u. During printing of the clay paste, the clay paste undergoes undrained shearing resulting in plastic deformation. The pressure required to shear the clay depends on the undrained shear strength of the clay. Conclusively, the printing pressure is more related to the LI rather than water content as S_u is directly related to LI.

2. Printing pressure is independent of clay types

   The printing pressure is directly related to S_u of the clay which is a function of the LI of the clay. As long as the LI and S_u of two different clay paste are equal, the extrusion pressure will be the same.

3. Shrinkage of the printed specimen is a function of the water content of the clay

   The void ratio(e) of the clay is given by $e = V_v/V_s$, where V_v is the volume of voids and V_s is the volume of the solids. When the clay is saturated, the voids are filled with water. When dried, only the volume of voids decreases which causes a decrease in the total volume of the specimen. For two different types of clay having total volume equal, the clay with higher water content will shrink more because of the higher volume of voids. Hence, the shrinkage of the printed specimens is a function of the water content of the clay paste during printing.

1.3 Research Objectives

The purpose of the thesis is to identify the factors that affect the extrusion pressure during the 3D printing of clay and to estimate the shrinkage of printed specimens post-printing. The specific objectives are listed below:

1. Develop a mathematical model relating printing pressure with geometrical parameters of a 3D printer and LI of clay.

2. Develop a mathematical model to predict the shrinkage of printed specimens based on moisture content.

3. Design an experimental procedure to determine optimum printing pressure to avoid under and over-extrusion.

1.4 Terminologies used

The landscape of 3D printing research is dynamic and ever-evolving, continually introducing new terms and refining existing ones. This evolution often results in interchangeability or subtle distinctions among terms used in academia, literature, and publications, which can cause confusion. Therefore, this thesis delves into the discussion of various terms to provide a clearer understanding of the methods and processes involved in 3D printing.

1.4.1 Nozzle travel velocity

Nozzle travel velocity or travel velocity refers to the speed at which the printing nozzle moves across the build platform or the previously printed layers during the 3D printing process. It determines how quickly the nozzle can traverse the printing area while maintaining precision and accuracy.

1.4.2 Print speed

Print speed also known as printing speed refers to the overall speed at which the 3D printer builds up the layers of the object being printed. It encompasses various aspects of the printing process, including the movement of the printer's nozzle or printhead and the rate of material extrusion.

1.4.3 Extrusion speed

Extrusion speed is the speed at which the printing material is extruded through the nozzle orifice during the 3D printing process. It represents the rate of material flow from the printer's extruder and is influenced by factors such as bid dimensions, moisture content, and nozzle size.

1.4.4 Threshold pneumatic pressure

Threshold pneumatic pressure is defined as the pressure required on the piston to initiate clay paste extrusion. It is related to the liquidity index and the geometry of the tank. This pressure is critical as it represents the minimum pressure required to begin the extrusion process effectively.

1.4.5 Operating pneumatic pressure

Printing Pressure refers to the pressure necessary during the actual printing process to maintain a consistent extrusion of the clay paste. This pressure ensures that the clay paste is extruded with sufficient force to achieve the desired shape and detail of the printed object, while also maintaining the structural integrity and quality of the output.

1.4.6 Net pressure

Pneumatic operation pressure is the difference between operating pneumatic pressure and the piston resistance in the clay tank.

1.5 Organization of Thesis Chapters

This dissertation comprises four chapters, including the introduction (chapter 1), literature review (chapter 2), journal article (chapter 3), and conclusion and recommendation of the research work (chapter 4).

1. The first chapter introduces the research question and states the purposes and objectives of the study. It briefly outlines the structure of the dissertation.

2. The second chapter presents the review of relevant literature to establish the context of the study. It identifies gaps and issues in the existing research that this study aims to address.

3. The third chapter is a journal article that presents a short introduction, and research methodology, including the research design, and data collection methods, and reports the findings of the research. It also presents the summary and conclusion.

4. The fourth chapter summarizes the key points and reinforces the significance of the study with some suggestions for future work to be continued after this research.

CHAPTER 2

LITERATURE REVIEW

Unlike traditional subtractive manufacturing methods, where the material is removed from a solid block to create a shape, 3D printing adds material layer by layer to build up the final object.

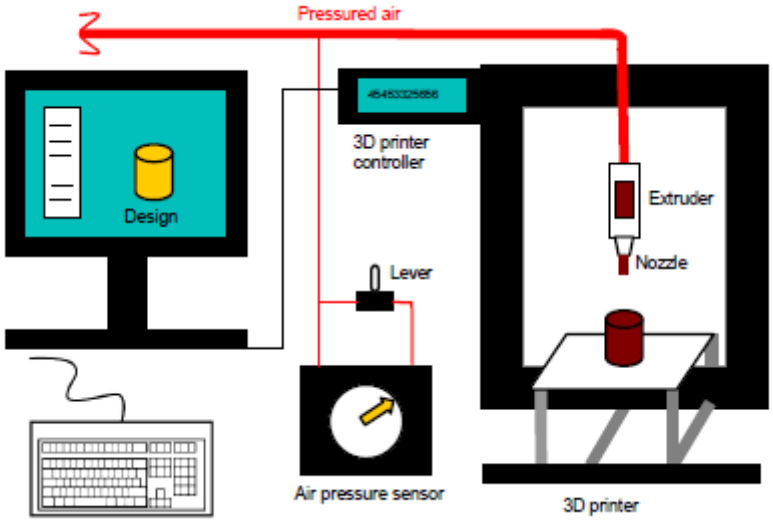

Figure 2.1: 3D printing mechanism [1]

2.1 3D printing process

The basic process involves design, slicing, printing, and post-processing. These steps are described below:

2.1.1 Design

The first step is to create a digital model of the object that needs to be printed. This can be done using any 3D modeling software or by scanning an existing object using 3D scanning technology. Fusion 360 was used in this research.

2.1.2 Slicing

The digital model is exported from 3D modeling software as an STL (Standard Tessellation Language) file and imported into any slicing software. The digital model is sliced into thin horizontal layers using slicing software. This creates a G-code having a set of instructions for the 3D printer to follow. There are various software available to generate g-code. Repetier and Cura are among the open-source ones while Simplify3D (not open-source) is another prominent one and also used in this study. G-codes can be written manually as well which gives an advantage over restrictions in software of equal heights [20].

2.1.3 Printing

The printer reads the G-code and builds objects layer by layer. There are various types of 3D printing technologies, including Fused Depositional Modeling (FDM), Liquid Deposition Modeling (LDM), Stereolithography (SLA), Selective Laser Sintering (SLS), and others, each with its own unique process and materials.

2.1.4 Post-processing

After printing, the object may require additional finishing steps such as removing support structures, sanding, painting, or other treatments to achieve the desired final appearance and functionality.

2.2 Benefits of 3D printing

3D printing has a wide range of applications across industries including manufacturing, ceramics, construction, aerospace, automotive, healthcare, fashion, and more. It allows for rapid prototyping, customization, and on-demand production of complex geometries that may be difficult or impossible to achieve with traditional manufacturing methods.

- The amount of material required is less than for a traditional subtractive method where the material is removed from a block until the part geometry is achieved [22].

- AM is capable of producing parts or objects that more traditional methods cannot easily do such as creating multi-material parts and biomedical objects including organs [23].
- AM can reduce the time and cost of manufacturing.
- AM allows rapid prototyping, customization, and on-demand production of objects.
- AM helps to get the work done in hazardous environments as well where the working of humans is not safe.

2.3 Types of AM for ceramics

Fused deposition modeling (FDM) using polymers, additive manufacturing of powders by selective laser sintering (SLS), selective laser melting (SLM) or liquid binding in three-dimensional printing (3DP), as well as inkjet printing, contour crafting, stereolithography, direct energy deposition (DED) and laminated object manufacturing (LOM) are the main methods of AM. These methods are briefly explained, their applications and suitable materials for each method are introduced, and their benefits and drawbacks are discussed.

2.3.1 Fused Deposition Modelling

The FDM method also referred to as fused deposition of ceramics (FDC), stands as one of the most prevalent 3D printing techniques. It was first developed by Crump et al., with a patent filed in 1989 [24], and later brought to the commercial realm by Stratasys Inc. in 1990 [25]. FDM involves the use of a continuous filament of a thermoplastic polymer to build up material layers during the 3D printing process Figure 2.2a. The filament is heated just above its melting point at the nozzle to attain a semi-liquid state before being extruded onto the platform or previously printed layers, where it immediately solidifies. Clearly, due to the inherent brittleness of ceramics, they cannot be shaped into flexible and

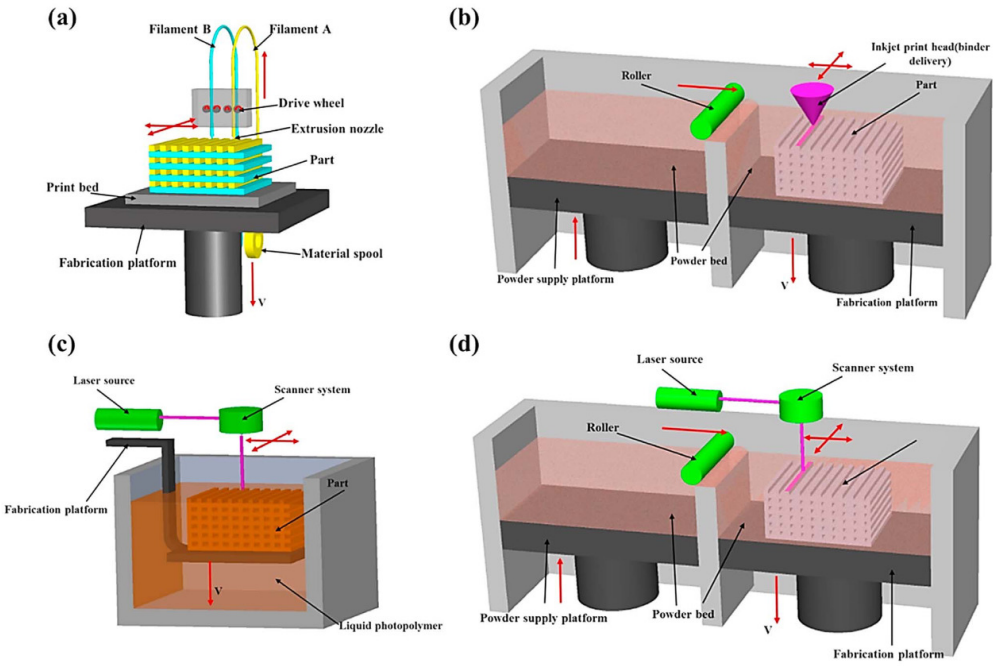

Figure 2.2: Major additive manufacturing methods: (a) fused deposition modeling; (b) inkjet printing; (c) stereolithography; (d) powder bed fusion [2]

windable wires for use as feedstocks. Therefore, composite filaments are prepared by densely loading ceramic particles (up to 60%) into thermoplastic binders for ceramic materials to be compatible with FDM [26]. Following the printing, akin to conventional FDM, the printed ceramic part undergoes binder removal and sintering to achieve densification. The first application of FDM to ceramic fabrication was reported by Danforth [27] at Rutgers University in 1995 using Al_2O_3- and Si_3N_4-filled binder systems.

The vertical dimensional resolution of the part is dictated by the layer thickness, which in turn depends on the nozzle size [28]. Key processing parameters affecting the mechanical properties of 3D printed parts encompass bid layer thickness, width, orientation, and air gaps within or between layers [29]. Inter-layer distortion, identified as a primary factor leading to mechanical weaknesses in these parts [30]. The stepping effect or staircase effect, which is also regarded as the major disadvantage of FDM, can be easily found in printed ceramic parts. While FDM offers advantages such as cost-effectiveness, speed, and simplicity, it also suffers from drawbacks including inferior mechanical properties, a layered

appearance, poor surface quality [31], and a limited range of usable thermoplastic materials [29]. However, the alignment of fibers, the adhesion between fiber and matrix, and the occurrence of voids present ongoing challenges in these composite parts [32, 33].

2.3.2 Inkjet printing and contour crafting

Inkjet printing, a key technique in the additive manufacturing of ceramics, is particularly useful for creating complex ceramic structures, like scaffolds for tissue engineering. In this process, a stable ceramic suspension, such as zirconium oxide in water [34], is pumped and dispensed as droplets from an injection nozzle onto a substrate. These droplets arrange themselves into a pattern that solidifies sufficiently to support subsequent layers Figure 2.2b. Notably, this method is celebrated for its swiftness and efficiency, offering significant flexibility in designing and producing complex structures and creating two-dimensional digital text and images [35].

The efficacy of inkjet printing of ceramics relies heavily on critical factors such as formulation of ceramic powder and ink, as well as their inherent properties, particularly rheological characteristics like dispersivity, stability, viscosity, and surface tension [26]. Moreover, maintaining a moderate pH level is essential to prevent potential corrosion of the jetting system by the ink. Ceramic inks often exhibit low viscosities, sometimes as low as a few mPa.s, due to low solid loading. This can lead to prolonged drying times and significant shrinkage, potentially compromising the final accuracy of the printed part.

There are two primary types of ceramic inks used: wax-based inks and liquid suspensions. Wax-based inks are melted and applied to a cool substrate to solidify, whereas liquid suspensions solidify through the evaporation of the liquid component. The quality of the inkjet-printed parts depends on various factors, including the particle size distribution of the ceramics, the viscosity and solid content of the ink, and the extrusion rate, nozzle size, and printing speed [36]. Challenges with this method include maintaining workability, achieving fine resolution, and ensuring adequate layer adhesion.

Contour crafting is used mainly for additive manufacturing of large building structures in which a concrete paste or soil is extruded using larger nozzles and high pressure. This technique has gained interest for potential construction applications, particularly in extraterrestrial environments such as the moon [37].

2.3.3 Stereolithography

Stereolithography (SL) is one of the most prominent and popular 3D printing technologies, first proposed and developed by Hull in 1986 [38] and later commercialized by 3D Systems Inc. This method employs UV light (or sometimes an electron beam) to trigger a chain reaction in a layer of resin or monomer solution. The monomers, typically acrylic or epoxy-based, are UV-sensitive and rapidly polymerize into chains upon activation (radicalization). This process leads to the solidification of a desired pattern within the resin layer to support subsequent layers Figure 2.2c. Any unreacted resin is typically removed after printing, and additional post-processing treatments such as heating or photo-curing may be applied to some printed parts to enhance their mechanical properties. In the production of ceramic-polymer composites, a dispersion of ceramic particles in monomers can be utilized [36], as well as polymer-derived ceramifiable monomers like silicon oxycarbide [39].

Ceramic SL has undergone extensive development and has found applications in fabricating both dense and cellular parts across various fields. These applications range from parts featuring complex microelectronic components such as sensors [40] and photonic crystals [41], to biomedical implants such as bone scaffolds [42] and dental components [43]. SL is renowned for its ability to produce high-quality parts with fine resolutions down to 10μm [33]. However, it is relatively slow and expensive, and the range of printable materials is somewhat limited. Additionally, the kinetics of the reaction and the curing process are intricate. The thickness of each layer is mainly controlled by the energy of the

light source and its exposure duration [44]. SLA is particularly effective for additive manufacturing of complex nanocomposites [45].

2.3.4 Powder bed fusion

Powder bed fusion processes involve the meticulous spreading and compact packing of fine powders in layers on a platform. Each layer's powders are then fused using either a laser beam or a binder, with subsequent layers added and fused to construct the final 3D object Figure 2.2d. Upon completion of printing, the excess powder is vacuumed off, and additional processing such as coating, sintering, or infiltration may be performed. The powder's size distribution and packing, which affect the part's density, are crucial for this method's effectiveness [46].

For powders with low melting or sintering temperatures, lasers are used, while others require a liquid binder. Selective Laser Sintering (SLS) involves partial melting, facilitating molecular-level fusion, while Selective Laser Melting (SLM) fully melts the powders, resulting in enhanced mechanical properties [47]. The feasibility of fabricating complex 3D ceramic parts using SLS was first demonstrated by Lakshminarayan et al. at the University of Texas at Austin in 1990 [200,201] utilizing Al_2O_3 based mixed powder systems. In 3D Printing using a liquid binder, factors such as binder chemistry, powder particle size and shape, extrusion velocity, and post-processing significantly influence the outcome [33, 46]. Binder extrusion typically results in higher porosity compared to laser-based methods, which can yield denser parts [46].

The primary advantages of powder bed fusion include fine resolution and high-quality printing, making it ideal for producing complex structures in various fields like tissue engineering, aerospace, and electronics. Additionally, its self-supporting powder bed facilitates the removal of supporting material. However, drawbacks include slow printing speed, high costs, greater shrinkage, and increased porosity when using binder fusion. Ceramic SLS is also an indirect multistep process wherein a sacrificial binder material is

used for the bonding of ceramic particles, which is then removed through debinding in a subsequent high-temperature firing process. Consequently, ceramic SLS is unable to produce fully enclosed structures as the untouched materials cannot be drained [26].

2.3.5 Direct energy deposition

In Direct Energy Deposition (DED), a focused thermal energy source heats a specific region of the substrate, melting a feedstock material (either powder or wire) at the same time. This melted material is then deposited and fused into the substrate, solidifying once the energy source moves away [48]. At the University of Birmingham, Wang et al. [49] successfully combined the FDM and DED into a hybrid process capable of fabricating $Ti_6Al_4V - TiC$ composite parts by feeding powder (TiC) and wire (Ti_6Al_4V) material into the focus of a CO2 laser.

The main difference between DED and SLM lies in the absence of a powder bed in DED, and the pre-melting of the feedstock before deposition, similar to FDM but with significantly higher energy for melting [26]. This renders DED suitable for tasks like crack filling or retrofitting parts where powder-bed methods are impractical. Moreover, it enables multi-axis deposition and the simultaneous use of multiple materials, easily integrating with traditional subtractive processes.

DED finds primary applications in manufacturing large, less complex components and repairing larger parts. Its benefits include reduced manufacturing time and cost, superior mechanical properties, controlled microstructure, and precise composition control.

2.3.6 Liquid Deposition Modeling (LDM)

Liquid Deposition is a material extrusion system, in which clay paste in a plastic state is extruded and deposited on a platform layer by layer at room temperature and solidified by evaporation of water or other solvents (Figure 2.3). The process has been referred to by various names in the literature, including extrusion freeform fabrication (EFF), aqueous-based extrusion fabrication (ABEF), filament-based writing (FBW), freeze

extrusion fabrication (FEF), direct ink writing (DIW), slurry deposition dispense plotting, bioplotting, rapid prototyping, robotic dispensing (RPRD), microextrusion freeform (MF), multiphase jet solidification (MJS), 3D fiber deposition (3DFD), and robocasting (RC) [36].

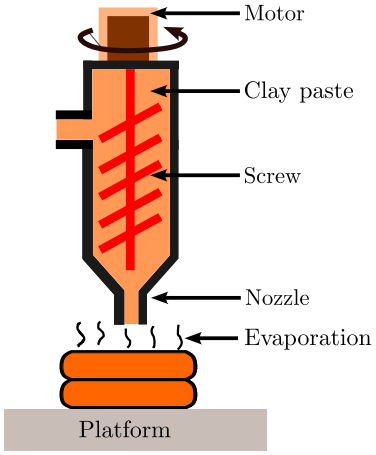

Figure 2.3: Liquid deposition modeling

LDM involves the precise placement of material emerging from an orifice onto a platform that provides a foundation for the initial layer. The material extruded from the nozzle with a circular cross-section adopts an elliptical shape on deposition [50]. The height of each deposited layer is fixed in the Z-axis defined in the slicer, but it can be controlled if the G-code is written manually [20]. The ratio of the paste extrusion speed and the nozzle speed in the XY plane determines the width of the deposited layer. The control of this ratio is crucial for maintaining precise overall dimensional accuracy, wall thickness, and uniform composition of each layer through proper alignment of deposited lines. Although the geometric and kinematic aspects of the process are determined by programmed parameters ensuring accurate execution, the flow of extrusion fluctuates due to the rheological characteristics of the material and its interaction with the extrusion apparatus. The material properties, layer height, and deposited width determine the minimum angle for self-supporting vertical walls. When this angle is exceeded, supports are needed for stability, requiring removal afterward.

The first experimental extruders were developed, along with the pioneer open-design and low-cost printers of the RepRap and Fab@Home projects, which were controlled by the open-source code electronics of the Arduino project [51]. Later, in 2014, it started being used at the commercial level with the initiatives of new companies (Lutum, 3DPotter, WASP, Zmorph Gaia) with much friendlier operating systems and reduced maintenance costs. Madrid [13] employed LDM to investigate the potential of using common clay in simple 3D printing machines for construction, highlighting its adaptability, potential for indefinite reuse, and suitability for producing various shapes. Clays, being one of the oldest materials used by humans, still play a crucial role in modern construction and infrastructure [52].

The extrusion of the clay paste can be controlled based on the type the extrusion method used. If an air compressor is used to extrude clay, changing the air pressure will affect the extrusion speed. If a mechanical extrusion system (usually in the form of a rod that is attached to a stepper motor) is used, changing the speed of the motor will change the extrusion speed, thus the amount of clay extruded at a given point in time. Printing with different layer heights, and changing the distance between the nozzle tip and the print base (nozzle height) are also possible explorations that affect the 3D printed outcome. The base of the 3D printers is usually flat and the 3D printers are kept stationary for precision purposes. However, these can be altered.

The process of extrusion involves the careful control of the material's properties, such as viscosity, to ensure it retains its shape during and after deposition. Post-printing processes may include drying and firing, which are crucial for the clay to gain strength and permanence. This technique has the potential to replace traditional production techniques for ceramic bodies, as the preparation of the input and subsequent operations are similar to those of conventional methods. The main advantages of LDM in the digitization of manufacturing processes include the elimination of investment in models, molds, and

matrices, the extension of morphological possibilities, and the speed and low production cost of individual pieces or small series [51].

2.4 Applications of 3D printing

Freedom of design, mass customization, waste minimization, and the ability to manufacture complex structures, as well as fast prototyping have revolutionized the applications of AM in various sectors. Recent developments have reduced the cost of 3D printers, thereby expanding their applications in schools, homes, libraries, and laboratories. Furthermore, in the construction sector, 3D printing is making significant strides.

The use of 3D printing has minimized the additional expenses that are incurred in the process of developing a product. AM can 3D print small quantities of customized products with relatively low costs. The growing consensus of adapting the 3D manufacturing system over traditional techniques is attributed to several advantages including fabrication of complex geometry with high precision, maximum material savings, flexibility in design, and personal customization. AM is capable of fabricating parts of various sizes from the micro-to macro-scale. However, the precision of the printed parts is dependent on the accuracy of the employed method and the scale of printing. 3D printing is devoid of the added cost due to mold making and tooling for a customized product. Some of the major applications of AM of clay are described in the following subsections.

2.4.1 Application of 3D printing in clay ceramics

3D printing has revolutionized the field of ceramics, enabling the creation of complex and intricate pottery designs that would be extremely difficult or impossible to produce using traditional ceramic techniques. Along with the development of computer technology, ceramic designers were encouraged to use a variety of new techniques to design ceramic models. By leveraging the capabilities of additive manufacturing, 3D-printed ceramics can now be fabricated with unprecedented levels of customization, efficiency, and

cost-effectiveness. For example, 3D Potter has introduced a line of ceramic 3D printers that use direct extrusion of real clay, allowing users to 3D print amazing ceramic designs that would not be possible with conventional methods [53, 54]. This technology is being widely adopted in architecture institutes, universities, and even high schools, where students can continuously print ceramic vessels and sculptures, marveling at the possibilities of this ancient art form combined with modern 3D printing [54]. Keep [3] explored 3D printing with different types of clay and printed amazing shapes (Figure 2.4) which is very difficult and expensive to produce with the traditional methods.

Figure 2.4: 3D printed objects from clay [3]

2.4.2 Clay ceramics for water treatment

Ceramic filters are highly favored for their extended durability, more flexible usage conditions, and reduced susceptibility to fouling. These filters, particularly effective in eliminating suspended solids, filamentous bacteria, and protozoa, owe their efficiency to the controlled pore size and porosity [55]. Ceramic materials are commonly used to manufacture many microfiltration membranes, which play a crucial role in household water purification systems to produce drinkable water. The production of ceramic filters typically

involves firing a composite 'green' body made from a blend of ceramic powder and a combustible material like rice husk or sawdust, which, upon burning, generates the necessary pores [56, 57]. He et al. [4] achieved a turbidity reduction of 83% for pond water using 3D-printed clay ceramics.

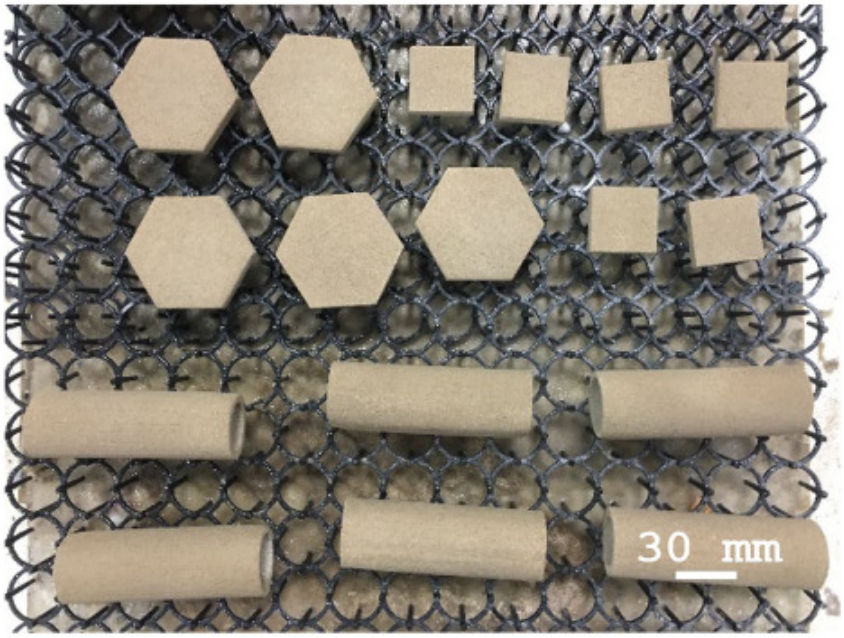

Figure 2.5: 3D printed clay ceramic membrane [4]

2.4.3 Clay 3D printing in the construction industry

Earthen construction stands as an ancient and pervasive form of vernacular building methodology. The onset of industrialization has gradually displaced these techniques, deeming them symbolic of construction in impoverished circumstances, eclipsed by the march of progress and the pursuit of enhanced well-being. But in recent times, earthen construction has garnered renewed attention within the construction sector, attributed to its minimal environmental footprint and recyclable attributes [58].

Earthen structures demonstrate a significant reduction in embodied energy during manufacturing compared to fired bricks or concrete [59]. Moreover, they contribute to a lower carbon footprint in construction [60] and exhibit high energy efficiency in operational

phases in contrast to conventional structures [61]. Finally, earthen materials also need less energy to recycle them [62]. Among recently introduced innovative approaches aimed at enhancing construction efficiency with earthen materials, digital-based construction techniques, notably 3D printing, emerge as particularly promising. The use of soil with the addition of some suitable stabilizers or binders in 3D printing will be a great choice for earthen construction. Initially, soil stabilization relied on natural stabilizers, incorporating elements like vegetable fibers [63] and biomaterials such as egg whites or proteins [64]. Subsequently, the practice evolved to incorporate industrial stabilizers like lime [65] and Portland cement [66].

One of the pioneering entities in the field of 3D printing with earthen materials is the Italian company known as the World's Advanced Saving Project (WASP). WASP has developed a specialized biocomposite for the stabilization of earthen mixtures [67]. This proprietary WASP biocomposite consists of a combination of rice husk (RH) and lime. It capitalizes on the abundant silica content in rice husk (RH) and takes advantage of the time-delayed bio-cementation effect facilitated by aerial lime, a result of lime carbonation [68]. As carbonation is an ongoing process with indefinite duration, its continual byproducts progressively enhance the mechanical properties of earthen mixtures over time [68], while also serving to protect the integrated vegetable fiber. WASP has designed and printed two full-size houses: (I) Gaia house and (II) Tecla house.

2.4.3.1 Gaia house

WASP collaborated with RiceHouse to build Gaia (Figure 2.6) in 2018, the first sustainable house model using local earth materials and natural waste from rice production. The construction of Gaia utilized a compound made of 25% on-site soil, 25% rice husk, 40% chopped rice straw, and 10% hydraulic lime [5]. This mixture was kneaded using a muller to create a homogenous and workable composite. The Crane WASP printer was designed to integrate natural ventilation, thermal-acoustic insulation, and building

systems within the same space. The precision and speed of 3D printing enabled intricate geometries that would be difficult to achieve with traditional construction methods. The 30 square meter printed area with 40 cm thick walls was completed in just 10 days. Gaia is highly energy-efficient and maintains a comfortable indoor temperature without the need for air conditioning or heating while having minimal environmental impact.

Figure 2.6: Gaia house printed with earthen materials by WASP [5]

2.4.3.2 Tecla house

The Tecla house (Figure 2.7) is a new circular model of housing entirely created with reusable and recyclable materials, primarily using local soil as the main building material. Designed by Italian architecture firm MCA and engineered by 3D printing specialists WASP, Tecla was 3D-printed in 2021 entirely from a mixture of local soil, water, rice husk fibers, and a binder. The house consists of two 4.2m tall, dome-shaped modules totaling $60m^3$, built over 200 hours using a multi-level, modular 3D printer with two synchronized arms. Tecla was developed as part of an eco-sustainability research study, aiming to produce low-carbon homes that leverage bioclimatic principles and vernacular architecture. This innovative construction process allows for the efficient use of natural materials while

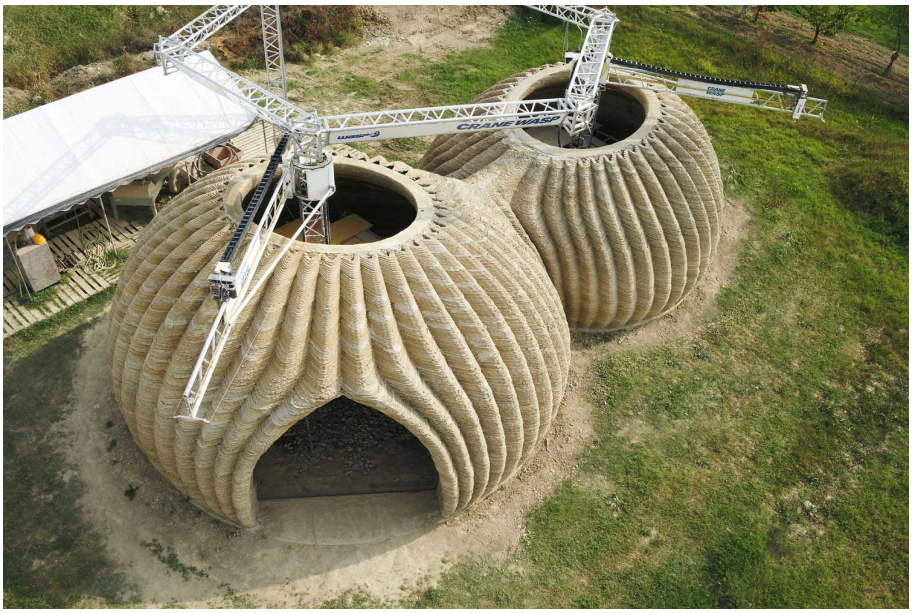

Figure 2.7: Tecla house printed with earthen materials by WASP [6]

significantly reducing typical construction waste. Indeed, in the spirit of a zero-kilometer construction, WASP's 3D-printing technology consists of the onsite printing of buildings, with the transportation of the 3D printer to the construction site.

Ferretti et al. [12] researched the load-bearing capacities of 3D-printed earthen wall of size 730 mm × 530 mm × 504mm (length × width × height) with bio-stabilized soil and investigated the failure mechanisms of the walls subjected to uniaxial compression tests. They achieved a compressive strength of 2.32 MPa proved to be satisfactory for a load-bearing earthen element fabricated through 3D printing, slightly surpassing the minimum compressive strength prerequisite for single-story external walls made of rammed earth (2 MPa) [69]. Many other researchers printed walls from soil and tested their mechanical performance and durability on a full scale. For example, Perrot et al. [14] 3D printed a 3-meter wall using an earth-based material with the addition of alginate seaweed biopolymer to increase its strength and improve productivity. They observed that on addition of alginate earthen material developed sufficient strength to sustain the weight of wall of 3m in 10hr while it took 50h without alginate. Dubor et al. [15] tested the structural and environmental performance of a full-scale 3D-printed wall of 2.85m high and

0.35m thick made of clay. Piani et al. [70] studied the effect of fibers in earthen bricks and found that bricks lacking fibers exhibit a brittle mode of failure whereas bricks that are reinforced with fibers demonstrate a more ductile mode of failure. Hamard et al. [71] reported that incorporating fibers serves as a reinforcement that helps to bind the material robustly, particularly at the junctions between walls or amongst consecutive segments in walls made of cob (mixture of clay, lime, sand, straw, and water). Alqenaee et al. [72] did an extensive study on cob printing demonstrating the challenges of transitioning from traditional cob construction to advanced computer-controlled 3D printing. They also provide insight into the environmental and economic benefits of usually locally sourced, natural materials in construction and the potential of 3D printing technology to create more sustainable and affordable housing.

Earthen construction materials are sustainable materials with several notable advantages, but their heterogeneous nature makes it challenging to standardize their strength and workability. The ability of a ceramic paste to be extruded is significantly influenced by its material composition and formulation, as these factors play a crucial role in determining the resulting plasticity [73]. To ensure workability and pumpability, it's essential to have an adequate amount of plastic clay to maintain viscosity and minimize friction within the soil mix [74]. The properties of the clay fraction largely dictate the overall flow characteristics of the mixture. Thus, analyzing the distinct clay fraction with water content for additive manufacturing is a crucial initial step in comprehending the behavior of the entire earth-based material blend.

The water content in clay is a critical factor in successful 3D printing with this material. Clay needs to have the right consistency - soft enough to be extruded through the printer nozzle, but not too saturated to lose its shape and structural integrity when printed [13]. Proper water content allows the clay to be easily fed into the printer and deposited in layers that can support themselves without deforming. Too much water can

make the clay too liquid and prone to slumping, while too little water results in clay that is too stiff and difficult to extrude [75].

Several studies have been performed to understand the clay behavior during extrusion either fully experimental or combinations of experimental or mathematical models or numerical analysis. For example, Calvert et al. [76] with their investigation on epoxy slurry reported that the variations in the cross-section of extruded filament occur with the change in nozzle movement speed under a constant nozzle set and extrusion velocity. When the nozzle speed is reduced, the adhesion between the filament and printing base gets stronger [77]. When the nozzle speed is reduced to half of the ideal value, the average bid width grows to double of designed value. Moreover, for mathematical modeling, there are several models developed to estimate extrusion pressure for ram extrusion but there is not any model for a pneumatic piston coupled with a screw (discussed in detail in Chapter 3). The present study develops the model by applying mass conservation and energy conservation (Bernoulli's equation) to the different components of the extrusion system to develop mathematical models for clay paste extrusion followed by the experimental program to validate those models. This study links the undrained shear strength of the clay with its water content, the widely used Atterberg limits, and printing parameters such as rate and bead geometry.

The drying period inherent to the extruded clay necessitates temporal considerations, thereby subjecting the printed objects to environmental factors and permitting post-printing manipulation. This opens up the possibility of incorporating the drying effects while designing the model before printing. In 3D printing with clay, shrinkage is of great concern. Shrinkage refers to the decrease in the volume of hardened clay resulting from moisture evaporation. It occurs due to the difference in relative humidity between clay and its environment and is exacerbated by higher water content, low relative humidity, high temperatures, and thin members, leading to crack formation [78]. Touati et al. [79] studied shrinkage on a 50cm wall (250 mm light earth materials and 25 mm cob) and

reported that shrinkage increases linearly with the decrease in water content of the wall. While there has been research on the shrinkage of 3D printed objects over time, this study specifically focuses on investigating the relationship between shrinkage and the initial moisture content during the printing process of the objects. This study aims to develop a shrinkage prediction model that takes into account the initial water content and SL of the clay. This model is intended to assist in determining the original size of the specimen to be printed, ensuring that the final dimensions of the object after drying align with the target specifications. This mathematical derivation of the shrinkage prediction model and experimental programs is discussed in Chapter 3 of this thesis.

CHAPTER 3

THE ROLE OF ATTERBERG LIMITS AND LIQUIDITY INDEX TO TUNE THE EXTRUDABILITY AND QUALITY OF 3D PRINTED CLAY OBJECTS

This chapter includes a journal article not published yet entitled: *The role of Atterberg limits and liquidity index to tune the extrudability and quality of 3D printed clay objects.*

This article is authored by: Rakesh Kumar Pandit and Luis Zambrano-Cruzatty.

Abstract: Additive manufacturing (AM), specifically 3D printing using earthen materials, offers a sustainable alternative to conventional construction practices and helps in reducing carbon footprint. 3D printing with earthen materials needs a proper investigation and study of clay (an important component of earthen materials) to be used in the mixture. The clay as a cohesive material works as a binding material in the mixture. This chapter elucidates the role of Atterberg limits and liquidity index in optimizing the extrudability and quality of 3D-printed clay objects. This study develops three mathematical models: the first one links threshold pressure on the piston to initiate clay paste extrusion with liquidity index and geometry of the tank; the second is the operating pressure prediction model linking printing pressure with liquidity index, extrusion velocity, bid height and width, and geometry of the equipment involved in the printing process; third for predicting post-drying shrinkage based on water content and Atterberg's limits. The screw extrusion model helps in predicting the printing pressure reducing the time and material loss by doing a trial to determine the printing pressure. The shrinkage prediction model allows for the pre-adjustment of printing dimensions to achieve the desired final product size, addressing the critical aspect of shrinkage management in earthen 3D printing. The research conducted an extensive experimental program with three different types of clay (Kaolinite, Cibas, and Presumpscot), using a WASP 40100 clay 3D printer to validate the model's predictions. The findings indicate that the liquidity index significantly

influences the extrusion pressure due to its correlation with the undrained shear strength of the clay. The study further explores the parameters affecting the flow rate during extrusion, highlighting the necessity of determining the optimal printing pressure to avoid under and over-extrusion of clay paste. The research confirms that extrusion pressure is more closely related to the liquidity index than to the water content alone, providing a reliable parameter for adjusting the 3D printing process. The study concludes with a recommendation for maintaining printing consistency within a liquidity index of 50-80%, correlating to a defined pressure range of 250-850 kPa with WASP 40100 clay printer for optimal 3D printing conditions. This research contributes valuable insights into the application of earthen materials in 3D printing, positioning it as a viable and environmentally friendly approach in the construction sector. Future studies are suggested to refine the model and extend its application to a broader spectrum of clay types and printing conditions.

3.1 Introduction

Additive manufacturing (AM) or 3D printing is a process that creates a physical object by the adhesion of layers from a digital model. Since its introduction, AM has evolved exponentially, driven in part by academia and because of the widespread accessibility of desktop 3D printers. In particular, liquid deposition modeling (LDM), which consists of depositing layers in a viscous fluid state at room temperature and subsequent solidification by evaporation of water or other solvents, has made possible the utilization of materials with the potential to revolutionize various sectors, including the construction sector [9, 10, 11, 12, 13]. AM stands at the intersection of technology and architecture, which has allowed the exploration of alternative and more sustainable construction materials that could partially replace concrete like earthen materials [5, 14, 15, 6]. Earthen materials with a high content of plastic clay are promising because they are abundant on the Earth's surface, have flowability when mixed with water, and have strong interparticle forces, which

can be enhanced by densification or cementation. This innovative approach blends the ancient practice of using clay as a building material with the precision and speed of modern AM techniques, promising an attractive alternative in the low-rise construction industry.

Despite the theoretical benefits of earthen materials and AM as a replacement for concrete and conventional construction methods, there are still barriers that could prevent their use. For instance, the reliability of the technology, the lack of construction codes, and a knowledge gap about the material's durability, strength, and maintenance. Furthermore, material processing challenges related to void formation, anisotropic behavior, and limited knowledge of how earthen materials will deform under gravitational loads drifting from the intended design [19].

It is worth mentioning that earthen materials can be outsourced in situ, downsizing the material's carbon footprint due to reduced transportation operations. However, this imposes a challenge in standardizing the strengths and workability of earthen materials due to the uncertain and heterogeneous nature of soils. Because of this, studies that determine the controlling parameters of earthen materials during the extrusion and short- and long-term curing are highly desirable.

Earthen construction materials are made of soil particles, and to ensure an optimum density, the grain size distribution must be well graded. The ability of a ceramic paste to be extruded is significantly influenced by its materials composition and formulation, as these factors play a crucial role in determining the resulting plasticity [73]. Also, to ensure workability or pumpability, there should be enough plastic clay to provide viscosity and reduce the friction associated with the soil mixture [74]. The clay fraction properties, macroscopically, control the fluidity behavior of the whole mix. Therefore, the characterization of the isolated clay fraction for AM is a valued first step toward understanding the behavior of the macroscopic earthen material mixture.

Benbow-Bridgewater [80] derived an equation relating extrusion pressure with the rheological properties of the ceramic paste. This model, widely used for ram extrusion,

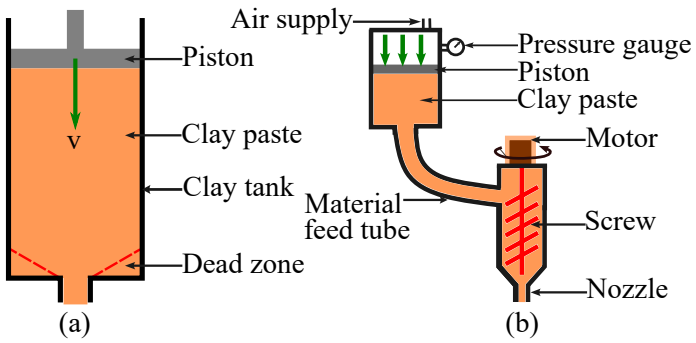

Figure 3.1: Extruder types: (a) Ram extrusion, (b) pneumatic piston with screw

connects the extrusion pressure and flow rate through the equilibrium of forces in a cylindrical container's wall and the paste's internal pressure. Guilherme et al. [73] demonstrated good agreement with measured and predicted values using this model. Later, Andrade et al. [81] developed another mathematical model for clay extrusion through a die of rectangular cross-section under steady-state flow. The primary parameters that influence extrusion pressure in this model encompass the effective stress during the compression of the clay paste, the geometry of both extrusion tools and filament, operational conditions, and the coefficients of friction between the barrel and the nozzle surfaces [81]. Tajiri et al. [82] modified the model from Andrade et al. for clay extrusion through a circular nozzle beyond a steady state called the coring point, also known as the dead zone of extrusion illustrated in Figure 3.1(a). They observed an acceleration of extrusion pressure beyond the coring point where the friction coefficient does not remain constant. Perrot et al. [83] also observed that the extrusion pressure increases when the piston reaches the dead zone. All the models above assume a steady piston velocity or steady flow rate. This assumption is invalid for pneumatic pistons, whose operating (printing) pressure remains constant. Furthermore, the models mentioned above will not work for hybrid (pneumatic piston with screw) extrusion mechanisms, where the clay is extruded from a feeder tank through a pipe towards a secondary screw extruder mechanism, as illustrated in Figure 3.1(b). Hu et al. [84] formulated a mathematical model for extrusion-based 3D printing of ceramic pastes for screw extrusion. He equated the volume of the paste flow at different sections of the

extrusion equipment but did not relate them with pressure nor provide the combined equation for the full extrusion system. The efficiency of energy utilization, the consistency of flux, and the appropriate extrusion pressure are influenced by both the extruder type employed (i.e., ram extruder, screw extruder, or both combined) and the plasticity of the clay paste [85]. The present study fills this gap by connecting mass conservation principles and Bernoulli's equation modularly to the different components of the extrusion system. Furthermore, this study links the undrained shear strength of the clay with its water content, the widely used Atterberg limits, and printing parameters such as extrusion rate and bid thickness.

This chapter's objective is to elucidate the role of Atterberg limits as controlling properties for the design and optimization of the printing process. This work shows that the liquidity index is a controlling state parameter that helps fine-tune the extrudability and quality of clay 3D-printed objects. An analytical 1D modular model that relates liquidity index, undrained shear strength, extrusion rate, nozzle diameter, and bid thickness with the pressure at the piston is derived to achieve the objective. An experimental program is conducted using three different clays with different Atterberg limits to measure the extrusion pressure given the flow rate, moisture content, nozzle diameter, width, and thickness of bid and compare the data from the analytical model.

The next sections deal with the role of Atterberg limits in AM and the derivation of analytical models. The fourth section explains full experimental procedures, including material preparation, extrusion tests, flow rate tests, and 3D printing of the specimens. The subsequent sections of the chapter contain a discussion of the strengths and limitations of the present models, and finally, conclusions of the study are presented.

3.2 Atterberg limits and consistency of clay for AM

Soil mechanics and clay behavior theory are fundamental to understanding the extrudability of clay materials. Changes in clay's water content significantly impact its

consistency, viscosity, and strength, directly affecting the outcome of the AM process. The consistency of clay has been extensively studied in the field of geotechnical engineering [86, 87]; for instance, Arthur Casagrande [88] adapted and standardized the consistency limits proposed by Atterberg [87], namely i) the shrinkage limit, ii) the plastic limit, and iii) the liquid limit. These so-called limits are water content thresholds where the material behavior of clay changes significantly. For example, the shrinkage limit (SL) is the water content that divides brittle solid from semisolid behavior, the plastic limit (PL) divides semisolid from plastic behavior, and the liquid limit (LL) separates plastic from liquid behavior (Figure 3.2). These parameters are easily determined using standardized tests described in ASTM D-4318 [89]. According to this standard, the Casagrande Cup test method is used to assess LL, while PL is generally determined via the thread rolling method. These limits serve as essential index parameters for classifying fine-grained soils and have demonstrated a strong correlation with various mechanical properties inherent to clays, including but not limited to the effective friction angle (ϕ'), undrained shear strength (S_u), compression index (C_c), and swelling index (C_s) [21].

Figure 3.2 shows the relationship between clay porosity (n) and void ratio (e) with water content to contextualize the use and importance of Atterberg limits in AM. The figure shows that as the gravimetric water content decreases, the porosity and void ratio decrease due to internal suction and capillary forces that shrink the clay volume. The water content in which the clay no longer changes its volume is the SL. The Liquidity index LI is shown below the water content axis in Figure 3.2 and is defined as.

$$LI = \frac{w - PL}{PI} \tag{3.1}$$

Where $PI = LL - PL$ is the plasticity index of the material. The LI maps the water content such that $LI > 1$ for $w > LL$, $0 \leq LI \leq 1$ for $PL \leq w \leq LL$, and $LI < 0$ for $w < PL$. Furthermore, an axis showing the undrained shear strength (S_u) illustrates the material's mechanical strength at different water contents. It is generally accepted that the

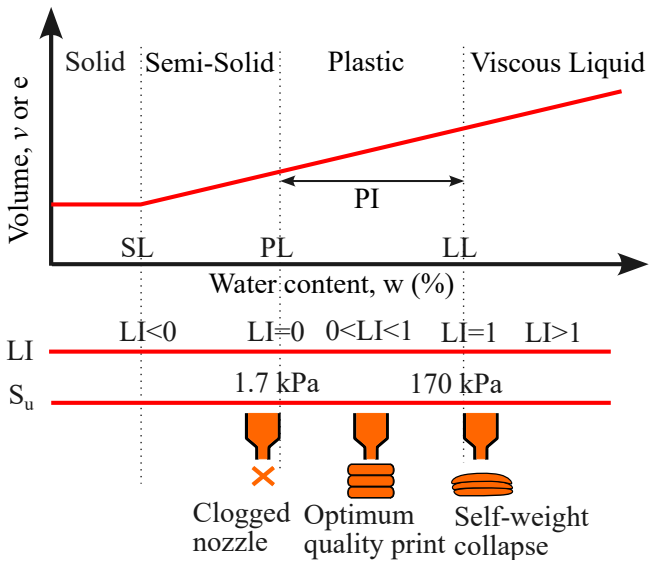

Figure 3.2: Schematic figure showing the influence of water content on the printability and quality of printed objects with clay. The Figure illustrates that for water content (w) larger than the liquid limit (LL), the printed object will collapse under self-weight and clog the nozzle below the plastic limit (PL). The optimal water content range is within the plastic and liquid limit, which ensures material extrudability and stability after printing.

LL occurs at undrained shear strength $S_u = 1.7$ kPa and that the strength increases if the clay loses water content such that $S_u = 170$ kPa at the PL [21, 90].

Figure 3.2 illustrates critical factors affecting clay printing. Printing with water content exceeding the liquid limit (LL) results in insufficient S_u to hold the shape of the printed object, causing collapse under its own weight. Conversely, attempting to print with water content around the plastic limit (PL) leads to nozzle clogging due to the need for higher extrusion pressures beyond the extruder's capabilities. Even if printed, poor layer adhesion occurs. Therefore, optimal clay printing requires balancing water content between PL and LL to achieve the necessary extrusion pressure while maintaining specimen stability.

The plastic range of clay, determined by its PI, spans the moisture content between the PL and the LL. The soil's plasticity index also influences extrusion pressure sensitivity. For example, in soils with a low plasticity index, even minor fluctuations in water content can significantly impact extrusion pressure due to substantial changes in the liquidity index and undrained shear strength.

Furthermore, the water content also affects other properties of soil, such as shrinkage. The specimen's shrinkage increases as the moisture content increases from the SL depicted in Figure 3.2. As a result, the true size of the specimen is not obtained as designed, and shrinkage effects must be carefully considered in cases where high-precision engineering is needed. Hence, it is crucial to consider these factors when optimizing clay formulations for 3D printing to ensure printing success, structural integrity, and quality.

3.3 Analytical Model

To relate extrusion pressure with the liquidity index of the clay paste and the geometrical parameters of the extrusion equipment, analytical models are developed for two conditions: (i) one-step extrusion (pneumatic piston only Figure 3.1 a) to estimate the minimum pressure required to initiate the flow of the clay paste in the tank, which is described in section 3.3.1; and (ii) two-step extrusion process (pneumatic piston with screw Figure 3.1 b) to estimate the operating pressure of clay paste driven by the piston pressurized with the compressed air and assisted by the screw in the extruder, which is described in section 3.3.2.

To derive those relations, the clay paste is assumed to be homogeneous, incompressible, and fully saturated, and the extrusion process is considered steady. The incompressibility assumption implies that the volumetric rate of clay material is constant for any section of the clay tank, feeder tube, or extruder. Furthermore, the extrusion rate is assumed to be significantly faster than the excess pore pressure dissipation rate, resulting in undrained behavior with shear at constant volume.

3.3.1 Threshold pressure to initiate clay paste extrusion

Figure 3.3 illustrates the longitudinal section of a clay tank having internal diameter D and orifice diameter d horizontally positioned, representing a tank similar to Figure 3.1a. The piston is placed at a variable distance $L + l$ from the nozzle, where l is the length of

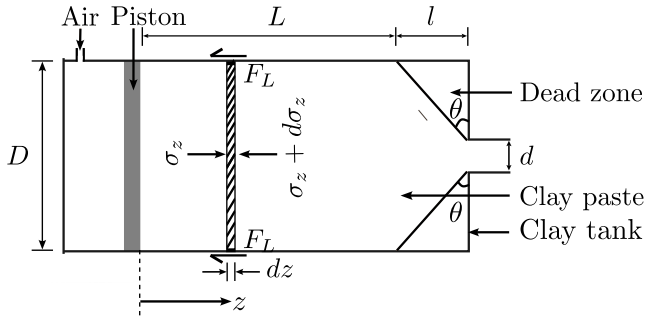

Figure 3.3: Clay extrusion at pneumatic threshold pressure

the dead zone, implying that L is a function of time. A differential clay disk is taken within the clay body in the domain characterized by L, and acting normal pressures $\sigma_z + d\sigma_z$ and σ_z are accounted on both sides of the element, where σ_z is the pressure at a distance z from the piston. Furthermore, lateral friction forces (F_L) are considered around the disk acting in a direction opposite to the movement of the piston. The dead zone is assumed to lie around the opening, inclined at an angle of angle of 45°. The lateral friction force can be estimated based on an adhesion concept as shown in Equation 3.2.

$$F_L = \alpha S_u \pi D_z dz \tag{3.2}$$

Where α is an adhesion factor, a value of 0.84 is recommended for soft clay [91]; S_u is the undrained shear strength of the clay, and D_z is the diameter of the tank at a distance z, which is $D_z = D$ for section $z = 0$ to $z = L$ and $D_z = d + 2(L + l - z)\tan\theta$ for the section $z = L$ to $z = L + l$.

Applying the equilibrium condition of forces on the differential element, Equation 3.3 is obtained.

$$\sigma_z A_z = \left(\sigma_z + \frac{d\sigma_z}{dz} dz\right) A_z + F_L \tag{3.3}$$

where $A_z = \pi D_z^2/4$ is cross-sectional area of the clay. Replacing Equation 3.2 into 3.3 we obtain Equation 3.4.

$$-\frac{d\sigma_z}{dz} = \frac{4\alpha S_u}{D_z} \tag{3.4}$$

To obtain an expression for pressure inside the tank with distance, Equation 3.4 is integrated from $z = 0$ to $z = L + l$ (see derivation of equations in Appendix C.1), resulting in Equation 3.5.

$$\int_{\sigma_p}^{0} -d\sigma_z = \int_{0}^{L+l} \frac{4\alpha S_u}{D_z}\, dz = \int_{0}^{L} \frac{4\alpha S_u}{D}\, dz + \int_{L}^{L+l} \frac{4S_u}{d + 2(L + l - z)\tan\theta}\, dz \tag{3.5}$$

Evaluating the pressure at $z = 0$ gives the piston pressure required for extrusion.

$$\sigma_p = \frac{4\alpha S_u L}{D} - \frac{2S_u}{\tan\theta} \ln\left(\frac{d}{d + 2l\tan\theta}\right) \tag{3.6}$$

Equation 3.6 represents the pneumatic on the piston to extrude the clay. It does not include the piston resistance. The undrained shear strength of the clay can be related to its LI by the Equation 3.7 proposed by Wroth and Wood [21].

$$S_u = 1.7 P_a exp(-4.6LI) \tag{3.7}$$

where P_a is the atmospheric pressure. Now, substituting S_u from Equation 3.7 and $\theta = 45°$ which also results in $d + 2l = D$ in Equation 3.6, Equation 3.8 is obtained.

$$\sigma_p = 3.4 P_a \left[2\alpha\left(\frac{L}{D}\right) - \ln\left(\frac{d}{D}\right)\right] exp(-4.6LI) \tag{3.8}$$

Adding piston friction resistance P_r to the above equation, the threshold pneumatic pressure (i.e. the minimum pressure by air on the piston to initiate the clay paste extrusion) is obtained as described in Equation 3.9.

$$P_{nt} = P_r + 3.4 P_a \left[2\alpha\left(\frac{L}{D}\right) - \ln\left(\frac{d}{D}\right)\right] exp(-4.6LI) \tag{3.9}$$

Equation 3.9 relates the threshold pneumatic pressure to (P_{nt}) to initiate the flow of clay paste with its liquidity index, the internal diameter of the tank, and the orifice diameter. Figure 3.4 shows the relation of (P_{nt}) normalized with atmospheric pressure with the change of different variables in equation 3.8. For instance, Figure 3.4(a) shows that the P_{nt} increases with the increase in α because of the increase in friction force on the walls of the container. Similarly, with the increase in the L/D ratio, the depth of clay increases by

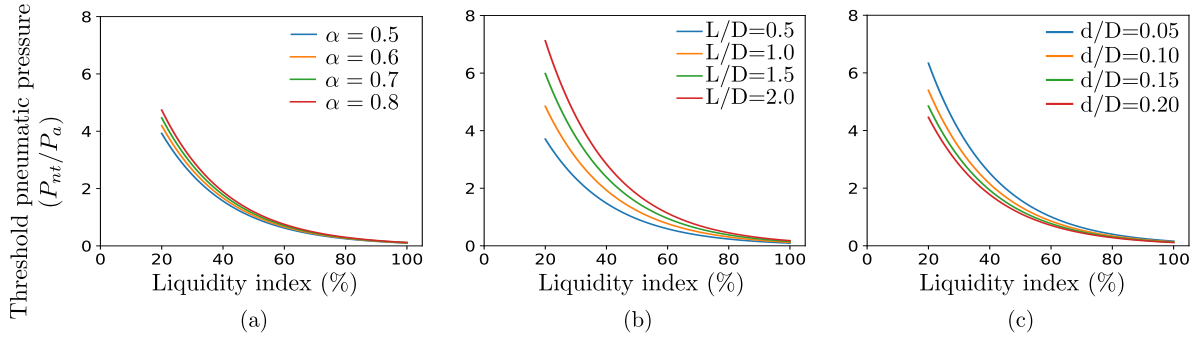

Figure 3.4: Pneumatic threshold (P_{nt}) pressure normalized with atmospheric pressure vs liquidity index for (a) different α and fixed $L = 0.1, D = 0.1, d = 0.015$ (b) different L/D ratio and fixed $\alpha = 0.84, D = 0.1, d = 0.015$ (c) different d/D ratio and fixed $\alpha = 0.84, D = 0.1, L = 0.1$. The theoretical results indicate low sensitivity to the adhesion factor and high sensitivity to geometrical configurations L/D and d/D.

a constant D (values of parameters are in the caption of Figure 3.4), which means more pressure is required to extrude the clay. Hence, P_{nt} increases with the increase in the L/D ratio seen in Figure 3.4(b). However, in figure 3.4(c), with the increase in the d/D ratio, the opening diameter increases for a constant D, which decreases the P_{nt}, meaning less pressure is required to extrude clay out of a larger opening compared to a smaller opening. All these figures show that P_{nt} is less sensitive to α, whereas geometrical configuration (i.e., L/D and d/D ratio) significantly contribute to the P_{nt}.

3.3.2 Operating pressure prediction model for pneumatic piston coupled with screw

Figure 3.5 illustrates the 3D printing mechanism of the two-step extrusion process. The same assumptions used to develop the threshold pressure model in section 3.3.1 are applied to derive this model, along with applying Bernoulli's equation. The prepared clay is filled in the tank, which is hung vertically with the other parts of the extrusion process attached, as shown in Figure 3.5. Level 1 represents the top height, whereas level 2 represents the bottom depth of the clay paste in the tank. Level 2 is also the connection point of the tank and the feeder tube. Level 3 represents the junction of the feeder tube and the extruder,

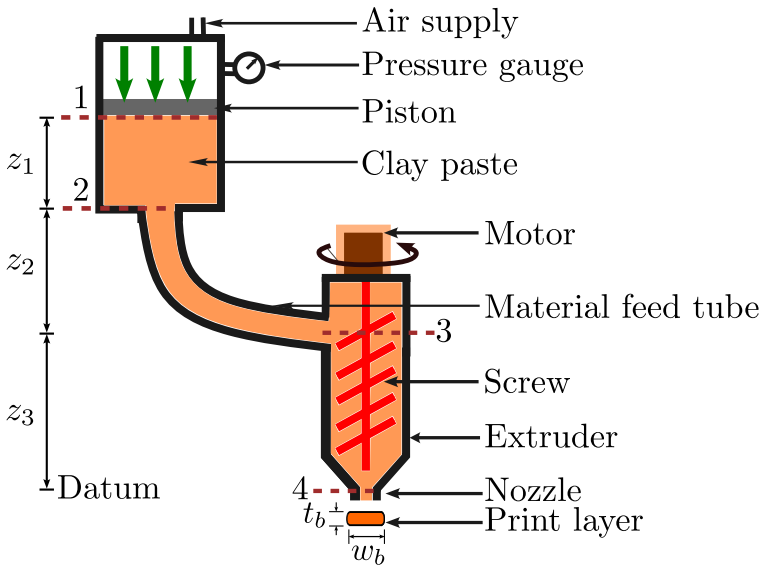

Figure 3.5: 3D printing mechanism for two-step extrusion process: pneumatic piston coupled with a screw. The numbers indicate reference elevations that relate printing parameters like bid width (w_b) and thickness (t_b) with pneumatic pressure and liquidity index.

while level 4 is the bottom level of the extruder. The height difference between each level is z_3 from level 4 to 3, z_2 from 3 to 2, and z_1 from 2 to 1.

Extruder consists of a screw shown in Figure 3.6 with diameter D_s, pitch W_s, flight depth H_s, flight angle θ_s and screw rotations per second ω_n. The velocity of extrusion v_e through the nozzle of diameter d_n relating to layer width w_b and thickness t_b is given by Equation 3.10 assuming the cross-section of the bid is $A_b = w_b t_b$ and using mass

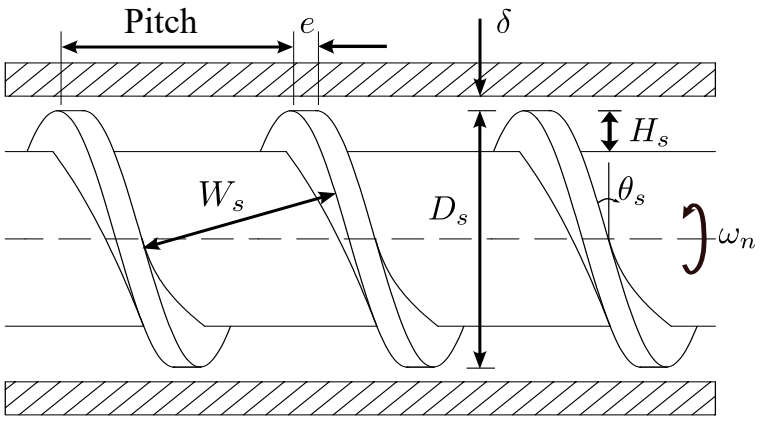

Figure 3.6: Geometrical parameters of the screw extruder.

conservation.

$$\frac{v_e}{v_t} = \frac{A_b}{A_n} = \frac{4w_b t_b}{\pi {d_n}^2} \tag{3.10}$$

where v_t is the travel velocity of the nozzle, and A_n is the area of the nozzle. Equation 3.10 shows that the ratio of the extrusion velocity to the travel velocity is equal to the ratio of the areas bid to the nozzle.

Continuity and Bernoulli's equation are applied between different levels in Figure 3.5 to derive a functional relationship between the pneumatic pressure, extrusion rate, bid geometry, and the liquidity index of the clay (see detailed derivation of the equation in Appendix C.2). The mentioned principles are applied between levels 3 and 4 (nozzle), leading to Equation 3.11.

$$P_3 = \gamma_t \left(\frac{v_e^2}{2g} + h_{l3} - z_3 - \frac{\left(\frac{d_n}{d_f}\right)^4 v_e^2}{2g} \right) \tag{3.11}$$

where, $\gamma_t = (1-n)\rho_s g$ is the bulk unit weight of clay paste, n is the porosity, d_f is the diameter of the feeder tube, and h_{l3} is the total head including friction loss in screw (h_{f3} obtained by dividing frictional force between the surface of the screw and clay paste by its unit weight) and contraction loss in the nozzle (h_{c3}) given in Equation 3.12 (see the derivation of the equation in C.3).

$$h_{l3} = h_{f3} + h_{c3} = \frac{\alpha S_u (2D_s W_s + 2H_s(D_s - H_s - W_s))}{(D_s H_s - H_s^2)\gamma_t} + \frac{K_3}{2g}\left(\frac{d_n^2}{d_{n1}^2} - 1\right)^2 v_e^2 \tag{3.12}$$

where, K_3 is contraction coefficient in nozzle, d_{n1} and d_n are diameters of nozzle base and nozzle tip respectively.

Subsequently, applying Bernoulli's equation and continuity equation between levels 2 and 3, Equation 3.13 is obtained.

$$P_2 = \gamma_t \left(\frac{P_3}{\gamma_t} + \frac{4\alpha S_u l_f}{\gamma_t d_f} - z_2 \right) \tag{3.13}$$

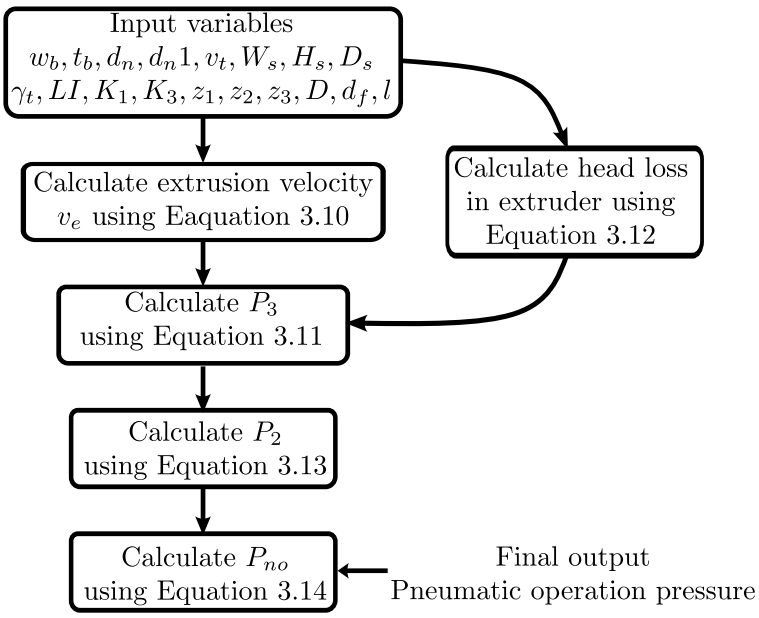

Figure 3.7: Flow diagram illustrating the order of equations to be solved to obtain operating pneumatic pressure at level 1

where l_f is the length of the feeder tube. Finally, Equation 3.14 is obtained when applying Bernoulli's continuity principles between levels 1 and 2.

$$P_1 = \gamma_t \left[\frac{P_2}{\gamma_t} - z_1 - \frac{v_e^2}{2g} d_n^4 \left(\frac{1}{D^4} - \frac{1}{d_f^4} \right) + \frac{K_1 v_e^2}{2g} d_n^4 \left(\frac{1}{D^2} - \frac{1}{d_f^2} \right)^2 + \frac{4S_u}{\gamma_t} \left[\frac{\alpha(z_1 - l)}{D} + \frac{2l}{(D + d_f)} \right] \right] \tag{3.14}$$

where D is the diameter of the clay tank, and K_1 is a coefficient at level 2 to account for energy loss due to contraction.

Equation 3.14 connects the optimum net pressure ($P_1 = P_{no} - P_r$) (which is operating pressure minus piston resistance) required to print clay paste to the depth of the clay in the tank ($L + l$), tank diameter (D), feeder tube diameter (d_f), nozzle diameter (d_n) and extrusion velocity (V_n) which is connected to the print layer thickness (t_b), width (w_b) and nozzle travel velocity (v_t). Figure 3.7 shows a flow diagram illustrating how to use the equations of this model to calculate the optimum operating pneumatic pressure needed to avoid under- or over-extrusion.

3.3.3 Shrinkage prediction model for clay

3D printing with clay presents an innovative approach to crafting intricate designs, yet it is susceptible to shrinkage post-drying. While common in clay-based manufacturing processes, this phenomenon poses a significant challenge to precision manufacturing and structural integrity. Shrinkage occurs as moisture evaporates from the clay during drying, reducing volume and creating potential distortions in the printed object's shape. Factors such as clay composition, ambient humidity, specific surface, and drying conditions can influence the extent of shrinkage, making it a critical aspect to manage throughout the printing and post-processing stages.

An obvious choice in predicting how much an object will shrink is using phase relationships and the shrinkage limit (SL) defined in section 3.2. First, the void ratio (e) and water content (w) are related by Equation 3.15.

$$Se = wG_s \tag{3.15}$$

where $S = V_w/V_v$ is the saturation defined as the ratio of the volume of water (V_w) to the volume of voids (V_v) of the clay, and G_s is the specific gravity of the clay minerals typically around $2.65 - 2.67$. Assuming all voids are saturated (i.e., $S = 1$), a linear relationship is formed between the void ratio and the water content, as shown in Figure 3.2. Thus, changes in the void ratio are due to changes in water content, as expressed in Equation 3.16.

$$\Delta e = \Delta w G_s \tag{3.16}$$

Here, the change in water content is equal to the difference between the water content during the extrusion process (w) and the shrinkage limit (SL), where the volume of the printed object remains constant; therefore, $\Delta w = SL - w$.

The volumetric shrinkage ($\Delta V/V_o$) is equal to the volumetric strain (ε_v), which is given by Equation 3.17.

$$\varepsilon_v = \frac{\Delta V}{V_o} = \frac{\Delta e}{1 + e_o} \tag{3.17}$$

where, e_o is initial void ratio and Δe is change in void ratio after desiccation. Replacing Equation 3.16 into 3.17, adding a fitting parameter α_s to account for the saturation deficit at the SL; leads to Equation 3.18.

$$\frac{\Delta V}{V_o} = \frac{G_s(\alpha_s SL - w)}{1 + wG_s} \tag{3.18}$$

Equation 3.18 shows that for the same water content, the clay with higher SL contracts less than that with lower SL after drying.

Finally, the linear scaling factor $S_f = l_o/l_f$ defined as the ratio of the originally printed length (l_o) to the shrunk length (l_f), is obtained as being directly proportional to the cubic root of the volumetric scaling factor as it is shown in Equation 3.19.

$$S_f = \frac{l_o}{l_f} = \beta \left(\frac{V_o + \Delta V}{V_o} \right)^{-1/3} = \beta \left(1 - \frac{G_s(\alpha_s SL - w)}{1 + wG_s} \right)^{-1/3} \tag{3.19}$$

where β is a constant that must be determined from the experiments. Equation 3.19 can be used to scale the object in the slicer to consider shrinkage effects.

3.4 Experimental program

In this study, three different clays are used to assess the model's validity. This section delves into the systematic procedures and experimental designs utilized to examine the relationship between Atterberg limits, liquidity index, and their impact on the 3D printing process of clay materials. Establishing a detailed framework for the experiments aims to shed light on the mechanisms influencing material behavior during printing. This provides a solid base for the analysis and findings. Starting with the subsequent sections, the chapter details the empirical efforts made to validate theoretical models and improve the extrudability and quality of 3D-printed clay objects.

3.4.1 Printer characteristics

The specimens are printed with a WASP 40100 clay 3D printer. 3D printing with delta type 3D printer WASP 40100 employs LDM technology, utilizing a pneumatic system for

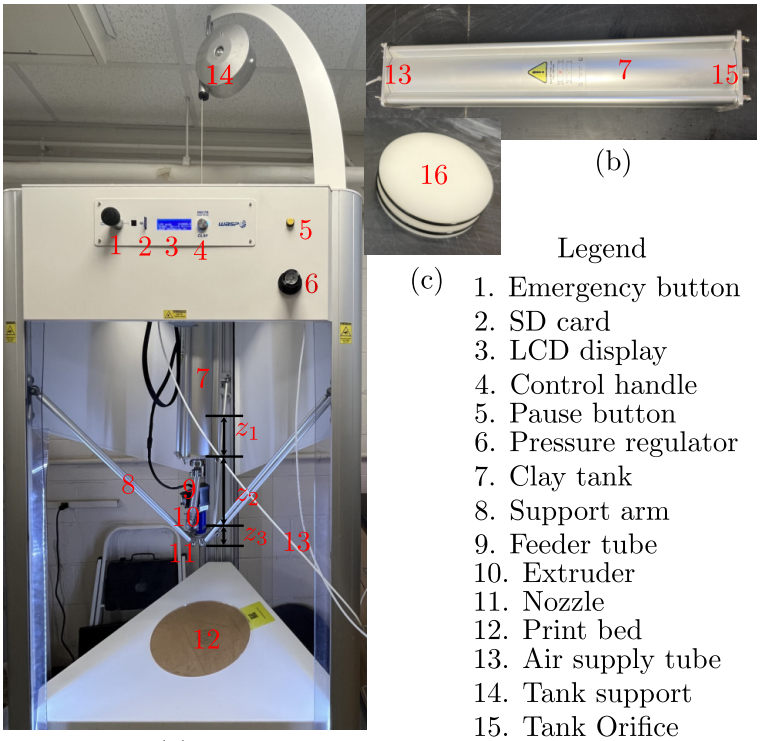

Figure 3.8: Annotated View of a Clay 3D Printing Setup: Identifying Key Components and Control Features: (a) WASP 40100 clay 3D printer (b) Clay tank (c) Piston

clay paste propulsion through a deposition arm. This integration of screw and pressure extruders in the LDM WASP extruder enhances precision and control over material flow, mirroring the accuracy seen in plastic polymer extrusion, and includes a retraction feature for stopping deposition when necessary.

The printer is 780 mm long, 850 mm wide and 1950 mm high. It consists of an outer frame made of metal sheet and Aluminium and the inner parts are tank, tank support, extruder, and support arm each labeled and shown in Figure 3.8. It contains a control panel with an emergency button, SD card door, LCD display, control handle, pause button, and pressure regulator. The clay tank is hung by the tank support above the printer and is connected to the extruder by a feeder tube. The clay paste is filled inside the tank and pressurized with air to push the material toward the extruder through the feeder tube. The clay in the extruder is dosed in a controlled manner by a screw and poured through an interchangeable nozzle in small quantities on the print bed. In this study, a nozzle of 2 mm

Table 3.1: Material properties of three different clays used in the experimental program of this study.

Clay Type	**LL (%)**	**PL (%)**	**PI (%)**	**SL (%)**	**% finer than 2μm**	**Activity**
Kaolinite	58	32	26	25.2	75.0	0.34
Cibas	44	21	23	17.3	52.1	0.44
Presumpscot	46	22	24	13	68.1	0.35

in diameter is used. The material is deposited layer by layer according to the instructions on the file made from the slicing software. It is therefore possible to make any shape and size of the objects within the limit of the printer.

3.4.2 Material properties

The clays used in the experiments are Kaolinite clay, Cibas clay, and Presumpscot clay. Ceramic suppliers produce the Kaolinite and Cibas clay, while Presumpscot is a natural clay. To characterize all the clays, PL, LL, and PI are determined using ASTM D4318 [89], and SL is determined using the water submersion method (ASTM D4943 [92]). Activity is calculated after determining the clay fraction using sedimentation analysis (ASTM D7928 [93]). Values are shown in the table 3.1. Low activity values reflect that all clays have a high content of Kaolinite. The first material is pure Kaolinite, while the second and third clay have other minerals too. It is observed that the Kaolinite clay has the largest liquid and plastic limits, which indicates that it requires more water in the mix to ensure printability. However, because all clays have similar plasticity indices, they are equally sensitive to changes in water content concerning the operating pneumatic pressure.

3.4.3 Material preparation

The clay is mixed with water above the LL for all experiments and left to saturate fully. It is left to dry close to the moisture content needed for the test. Then, it is mixed in a KitchenAid mixer for about 15 minutes until the mixture becomes homogeneous. The mixture is stored in a container sealed with plastic for 24 hours to ensure that samples are

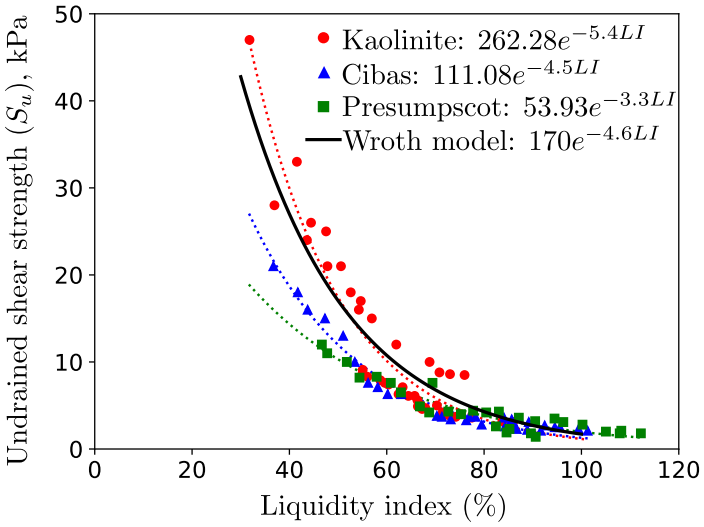

Figure 3.9: Coparision of undrained shear strength (S_u) of the clays with Wroth model: S_u for Kaolinite is highest among the tested soils and aligns well with Wroth model while it is low for Cibas and lowest for Presumpscot clay

left for a day to stabilize before carrying out the experiments. The homogeneity of the paste constitutes a fundamental parameter that critically affects the quality of the hardened extrudates as well as the operational efficiency of the extrusion process. The samples are prepared with different moisture content between PL and LL.

Fall cone tests are performed as per The British Standard (BS 1377:1990) to determine the clay's undrained shear strength. The test results are presented in Figure 3.9. Each clay is then subjected to further extrusion, shrinkage, and flow rate tests at a different moisture content.

3.4.4 Validation of Analytical Models

3.4.4.1 Extrusion tests

Extrusion tests are performed to verify the model derived in section 3.3.1 to determine the threshold pressure required to initiate the movement of clay in the clay tank. This validates the expression proposed by [21] to link undrained shear strength, liquidity index, and water content.

All three types of clay mentioned in the material preparation are used for the extrusion tests. The nylon piston (Figure 3.8(c) is lubricated with lubricating oil and placed inside the tank at a depth of 75 mm for all prints to keep L/D constant for all tests. Then, the tank is fully sealed, with the vent for air supply and the orifice for extrusion left open and laid horizontally on a table 3.8(b). The air is supplied from the left side of the piston (Figure 3.3), and its flow is controlled manually by the pressure regulator mounted on the printer.

Before each extrusion test, the piston friction force P_r is obtained by gradually increasing the pneumatic pressure until the nylon piston moves towards the right. The pneumatic pressure is recorded using a pressure transducer with a resolution of 0.01 kPa connected to an Arduino board sampling at a frequency of 2 Hz. The piston friction was not always constant, with values oscillating from 18 to 30 kPa (an average value of 24 kPa used for P_r in the model). This is attributed to the thermal expansion of the o-ring on the piston under repeated use.

The prepared clay is made into balls compressed by hands to remove air bubbles and plugged into the tank in three layers, filling one-third of the space at a time and subsequently pressing. Then, the tank is sealed, and air pressure is supplied gradually until the clay is observed to move out of the opening. The pressure at this stage is the threshold pneumatic pressure (P_{nt}) required to initiate the flow of clay paste, including the piston resistance. At this stage, the clay undergoes undrained shearing in a conical shape around the opening. After measuring the threshold pressure, all the clay is extruded from the tank. Clay samples are collected from three locations of clay paste in the tank, bottom, middle, and top, for the moisture content measurement. The average of the three measurements is recorded as the moisture content for that particular test. In total, 150 extrusion experiments were conducted; 50 for the Kaolinite, 50 for the Cibas, and 50 for the Presumpscot clay.

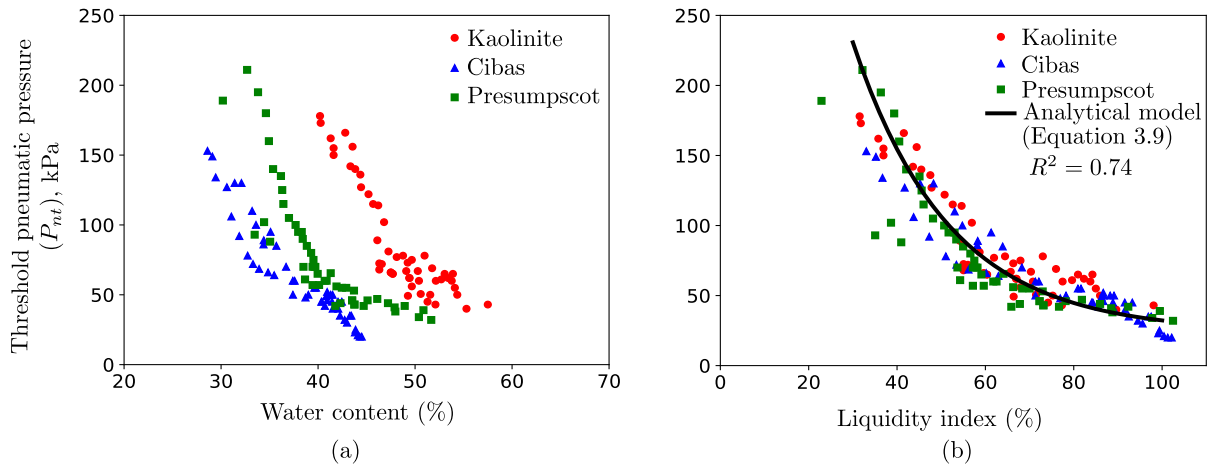

[h]

Figure 3.10: Threshold extrusion pressure with water content and liquidity index (a) Threshold extrusion pressure vs water content indicating distinct behavior for each clay used in this study (b) Threshold extrusion pressure vs liquidity index showing that Wroth's model links S_u, w and LI well. In this space, all data collides into a single region as predicted by Equation 3.9.

P_{nt} is plotted against water content in Figure 3.10(a) and LI in Figure 3.10(b). It is observed that when plotted against water content alone, three distinct curves are obtained for each soil. However, Figure 3.10(b) shows that all curves collide into a single region well described using Equation 3.9 with a coefficient of determination $R^2 = 0.74$. This indicates that using the Wroth model (Equation 3.7) to link S_u and LI works adequately for the extrusion process and validates its use for AM characterization.

3.4.4.2 3D printing tests

To validate the analytical model developed in section 3.3.2, 3D printing experiments are conducted using the three clays. The experimental outcomes are then compared with the predictions from the analytical model. For testing the mathematical model, a solid cylinder with a diameter of 50 mm and a height of 20 mm is designed in Fusion 360. It is then exported as an STL file into Simplify3D for slicing. The model is sliced with a 2mm nozzle profile. The major parameters of the slicer are:

Table 3.2: Slicing parameters used in the Simplify3D to slice the model.

Slicing parameters	**Values**
Bid width	2 mm
Bid overlap	1%
Extrusion multiplier	1
Infill pattern	Rectilinear
Infill percentage	100%
Travel velocity	25 mm/s

Before starting the print, the piston resistance is added to the pressure predicted by the model (Equation 3.14), and the total pressure (operating pressure) is set on the printer. Then, the material is slowly extruded. When the material is seen coming out of the nozzle, extrusion is stopped, the nozzle is wiped off, and printing of the cylinder is started. If the operating pneumatic pressure is predicted correctly, the bids and the printed object are consistent with the slicer parameters. If the pressure is too low, the material is under-extruded, which is evident if a gap is seen between the printed bids 3.11(a). Otherwise, if the pressure is too high, it over-extrudes material, which becomes evident if the printed bids overlap excessively 3.11(c) and results in the formation of the crest. The printing pressure increases or decreases based on the under-extrusion or over-extrusion. When the printer prints a 50 mm diameter solid, the pressure is recorded as the printing pressure. The diameter of the printed specimen is confirmed to be 50 mm when there is no

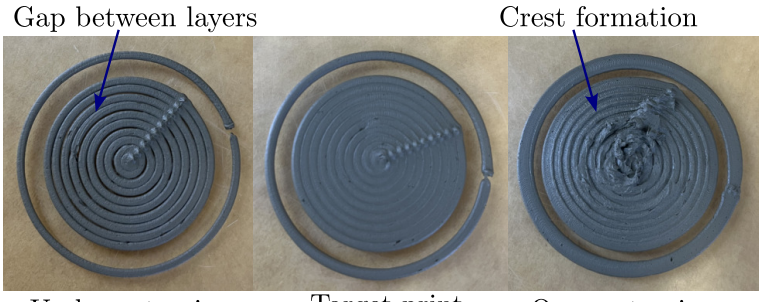

Figure 3.11: Effect of pressure on printing (a) Lower printing pressure than optimum causes under-extrusion of material resulting in the formation of gaps between layers (b) Optimum pressure results in good target print (c) Higher printing pressure than optimum causes over-extrusion of material resulting in excessive overlaps and formation of crest

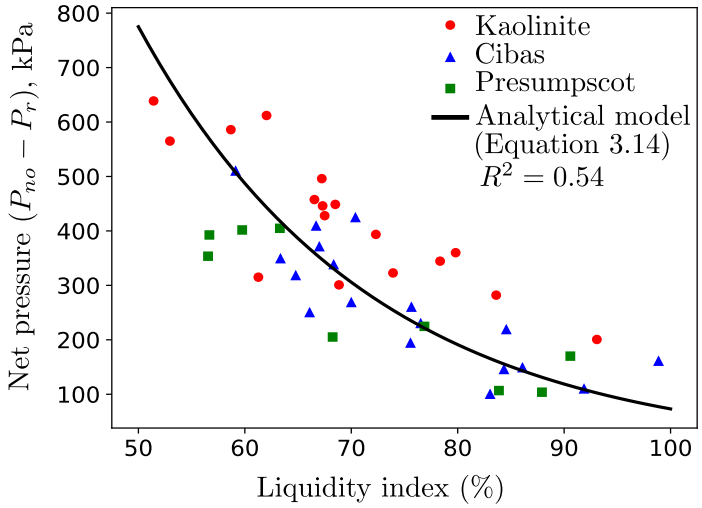

Figure 3.12: Relationship between printing pressure and liquidity index for 3D printing using a two-step piston plus screw extruder. The dots correspond to data obtained when a cylinder of 50 mm and 20 mm height was printed successfully at specified dimensions. The continuous line shows the predicted pneumatic pressure. Although all data show a similar trend, the model over-predicted the pressure for the Presumpscot clay, underpredicted for the Kaolinite clay, and has a reasonably good agreement for the Cibas clay.

gap or overlap between the layers and is also verified by measuring with a stainless steel ruler.

The values used for the contraction coefficients K_1 and K_3 in the model are 0.5 and 0.02 respectively [94]. The net pressures (after subtracting P_r from P_{no}) are plotted with the pressures obtained from the mathematical model in section 3.3.2 against LI in Figure 3.12. Figure 3.12 shows that the pressure increases for each clay with the decrease in LI (i.e., increase in S_u) as expected. The model underestimates Kaolinite's printing pressures, whereas it overestimates Presumpscot clay but fits reasonably well with the Cibas clay. This is because the S_u for Kaolinite at a certain LI is higher, and that for Presumpscot clay is lower (Figure 3.9). The proposed model produced $R^2 = 0.54$, although calibrating parameters for each clay could improve this.

From the 3D printing experiments, it is observed that, for the same LI, the models can be printed with lower pressure with either an increase in extrusion velocity, a decrease in nozzle travel velocity, or decreasing layer thickness.

3.4.5 Flow rate test

Understanding the extrusion behavior of clay is paramount for achieving consistent and high-quality prints. Variations in printing parameters, particularly operating pneumatic pressure (P_{no}), can significantly impact the flow rate of the material during printing. Figure 3.13 shows that deviations from optimal extrusion conditions may result in under-extrusion, where insufficient material is deposited, or over-extrusion, characterized by excessive material deposition. As explained in the previous section, these problems lead to structural defects and compromised print quality.

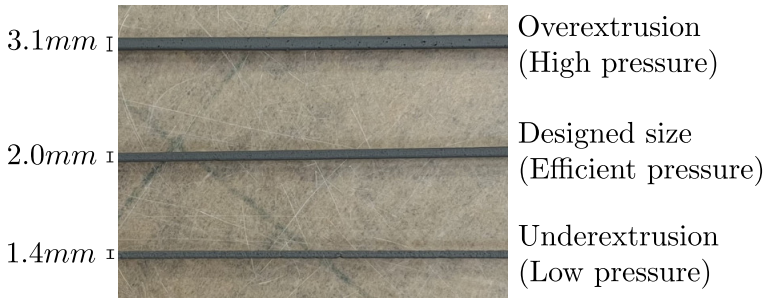

Figure 3.13: A visual guide to flow rate adjustments in 3D printing

The flow rate tests are simple and repeatable and help to calibrate the mathematical procedure in section 3.3.2. It consists of printing a single bid of length 250 mm, width 2 mm, and height 1 mm at a predefined nozzle velocity. Therefore, using Equation 3.10, the velocity of extrusion and the extrusion rate that guarantees the bid dimensions are known. As Figure 3.15 explains, this velocity leads to a predicted operating pneumatic pressure that can be compared with the actual operating pneumatic pressure, resulting in the desired bid width and thickness. The printing parameters are the same as in the section 3.4.4.2. The pressure on the sensor is set to lower than the predicted from Equation 3.14, and the printing is started. The bid is collected in a container of known weight and again weighed to calculate bid weight. This process is repeated 5-6 times by changing the pressure starting lower than predicted and stopping at higher than predicted. A Witmotion accelerometer sensor is used to record the extrusion time accurately. The flow rate required to print a layer of 250 mm×2 mm×1 mm in 16.38s (printing time) is $30.5mm^3/s$. However,

it was found that the measured printing time did not change significantly compared to the time predicted in the slicer. This process is repeated for various water contents and pneumatic pressures. A total of 13 tests are conducted; 4, 4, and 5 for the Kaolinite, Cibas, and Presumpscot clays, respectively.

The unit weight of the clay is calculated based on the moisture content using Equation 3.20.

$$\gamma_t = \frac{G_S(1+w)}{1+e}\gamma_w \tag{3.20}$$

where G_s is the specific gravity of soil solids, w is water content, γ_w is unit weight of water and e is the void ratio. Substituting e from $Se = wG_s$ and assuming fully saturated clay, 3.20 changes to Equation 3.21.

$$\gamma_t = \frac{G_S(1+w)}{1+wG_s}\gamma_w \tag{3.21}$$

Then, the clay volume (V) is calculated from the collected weight (W) of the extrudate using Equation 3.22.

$$V = \frac{W}{\gamma_t} \tag{3.22}$$

The volume of the extruded clay divided by the extrusion time gives the flow rate of the clay through the nozzle.

Figure 3.14 shows the results of the flow rate experiments for the Kaolinite (Figure 3.14(a)), Cibas (Figure 3.14(b)), and Presumpscot clay (Figure 3.14(c)). It is observed that the flow rate increases with the P_{no} for all clays regardless of the printing LI. In all plots, a horizontal black line indicates the target flow rate (i.e., 30.5 mm^3/s). Pressure above that results in over-extrusion, and below it results in under-extrusion (Figure 3.13). The intersection of the different curves with the target flow line indicates the operating pneumatic pressure that would result in the targeted flow rate.

The net pressure needed for the target flow rate can be plotted vs. the liquidity index, as shown in Figure 3.15 (stars symbols), which contains the results obtained from the 3D printing tests (dots). It is observed that the data from the 3D printing and the flow rate

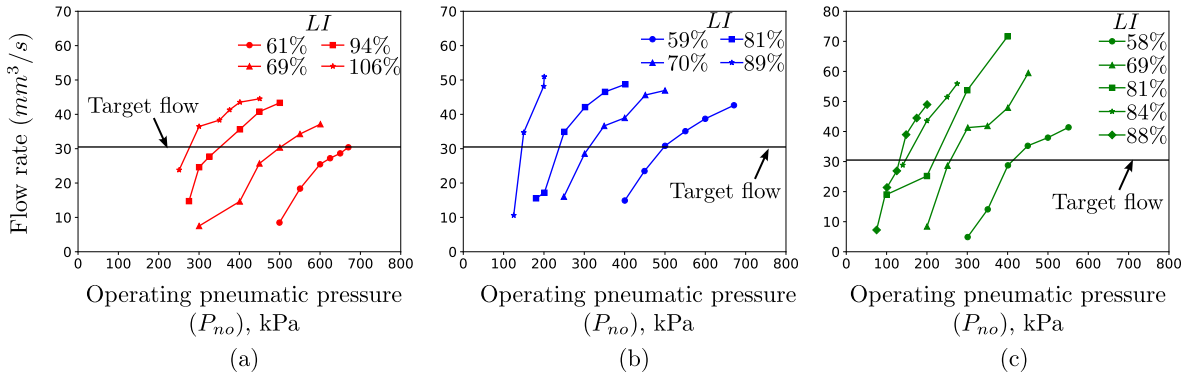

Figure 3.14: Flow rate test for three clays at different LI: Printing bid 250mm long, 2 mm wide and 1 mm high (a) Flow rate vs P_{no} at different LI for Kaolinite (b) Flow rate vs P_{no} at different LI for Cibas (c) Flow rate vs P_{no} at different LI for Presumpscot

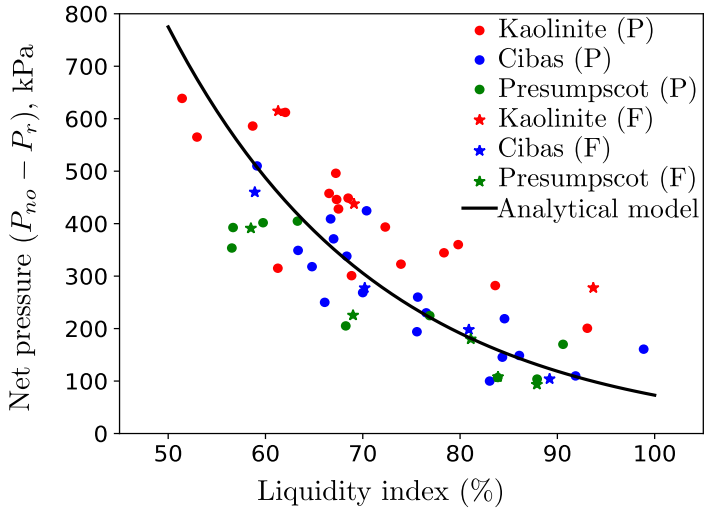

Figure 3.15: Comparison of net pressure from the 3D printing and flowrate tests vs. LI. It is observed that the calibrated model produced a reasonably good agreement between predicted and observed POP (P and F in the parenthesis represent the pressure from 3D printing tests and flow rate tests respectively).

tests both provide consistent results regarding the predictive power of the model presented in Figure 3.15 respectively.

It is worth noting that the flow rate tests are easy and inexpensive to perform and produce consistent results when compared with the 3D printing tests and the model. Therefore, it is recommended to perform flow rate and extrusion tests to calibrate model parameters rapidly.

On further analysis of the flow rate curves in Figure 3.14, it is observed that the flow rate increases with increasing pressure but at a decreasing rate, as indicated by the declining slope of the curves. This suggests that the relationship between pressure and flow rate is nonlinear and could be subject to diminishing returns as pressure increases. The potential reason for this may be the extruder's ability to try to deliver a consistent amount of material during printing. The other reason can be clay being a non-Newtonian fluid may exhibit shear-thinning behavior—its viscosity decreases with an increased shear rate. After a certain point, the rate of viscosity reduction can slow down at higher shear rates, leading to a decreased rate of increase in flow despite higher pressures [95]. However, this is less likely to happen because of the smaller shear rate during printing.

3.4.6 Shrinkage test

Shrinkage tests are performed for Kaolinite and Cibas clay on printed solid cylindrical models of diameter 50 mm and height 20 mm (Figure 3.16(a)) with different water content to calibrate parameter α_s in Equation 3.18. After printing, the specimens are left to air-dry for one day and then oven-dried for another day. The volume of the dried specimen is calculated using the water submersion method (ASTM D4943 [92]). The specimen is weighed to calculate dry mass, then tied to a string and dipped in wax at $100°C$ to have a uniform wax coating over the surface. The wax's weight is the difference between the final and initial weights of the specimen. Then, the specimen is dipped into a container of known volume, filled with water, and the weight of the whole setup is recorded. The water weight in this setup is subtracted from the weight of water in the container filled with water only. The volume of the displaced water and wax subtracted from the container's total volume results in the specimen's volume. The difference between this volume and the specimen's original volume divided by the original volume is the volumetric shrinkage.

The percentage volumetric shrinkage is plotted against the water content in Figure 3.17. Figure 3.17 shows that the shrinkage increases with the increase in the water content.

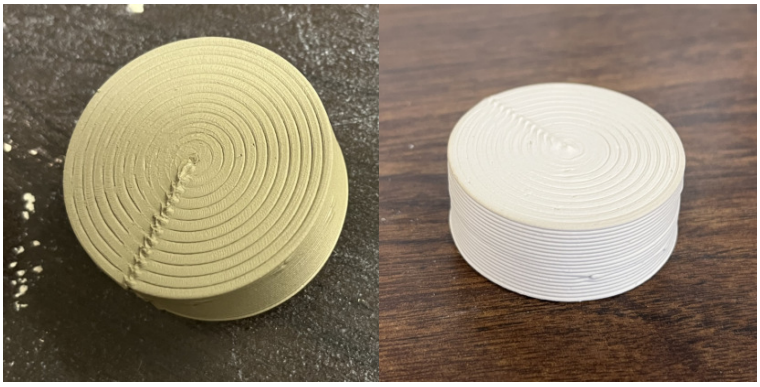

(a) (b)

Figure 3.16: Shrinkage test specimens (a) solid cylinder just after print (b) solid cylinder after complete drying

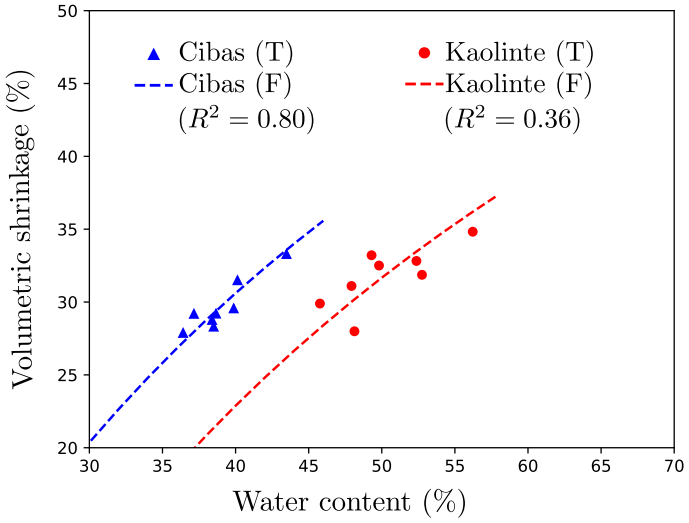

Figure 3.17: Shrinkage test data vs water content and shrinkage model fitted by RMSE method by changing α_s (T and F in the parenthesis represent the volumetric shrinkage results from test and curve fitted on the test data respectively)

The fitting parameter α_s in Equation 3.19 is determined by minimizing the root mean square error (RMSE) through error optimization. The model, incorporating the optimized α_s, is then plotted in the same figure3.17. The shrinkage limit used in the equation is given in table 3.1. The values of α_s for Kaolinite and Cibas are 0.8815 ($R^2 = 0.36$) and 0.9369 ($R^2 = 0.80$) respectively obtained by fitting the model (Equation 3.18) to the experimental data.

As an application of this model, specimens of different sizes (63mm dia.×24mm, 42mm dia.×16mm, 40mm dia.×20mm) are printed. The shrinkage for these specimens is predicted based on the water content and compared with the measured dimension in Figure 3.19b. Values of β are back-calculated using Equation 3.19 and plotted vs. the water content in Figure 3.19 based on diameter and height change. The back-calculated β values range between 0.95 and 1.05; with β being smaller for the height measurements. This is attributed to the different boundary conditions of the surfaces, which prompted more rapid desiccation through the curved lateral face and the top face than in the bottom face that was in contact with a semi-permeable surface. Nevertheless, based on the small change of β, posterior analysis is conducted assuming $\beta = 1$.

Equation 3.19 is used to predict the final dimension if the initial dimension, water content, and SL are known. The calculations are clay-specific because of different SL. Equation 3.18 is used to predict the volumetric shrinkage based on the water content and shrinkage limit of the clay. And the measured volumetric shrinkage is the difference between the printed volume and dried volume normalized with the printed volume. These predicted and measured volumetric shrinkage are plotted in Figure 3.18a. If the model predicted precisely all the points should align on the 1:1 median line. The model seems to predict well for Cibas clay while it varies for Kaolinite. The error in volumetric shrinkage prediction is calculated using Equation 3.23.

$$E_{vol} = \frac{(\Delta V/V_0)_p - (\Delta V/V_0)_m}{(\Delta V/V_0)_m} \times 100\% \tag{3.23}$$

where, $(\Delta V/V_0)_p$ is predicted volumetric shrinkage and $(\Delta V/V_0)_m$ is measured volumetric shrinkage. The error is less than 20% for Cibas clay which decreases with an increase in water content while it varies for Kaolinite between 0 and 30%. Later, the linear dimensions from predictions and measurements are compared. Figure 3.19b shows that the measured dimensions align reasonably well with the predicted ones. On closer observation, the diameter in Cibas clay and height in Kaolinite aligned well with the 1:1 line, meaning

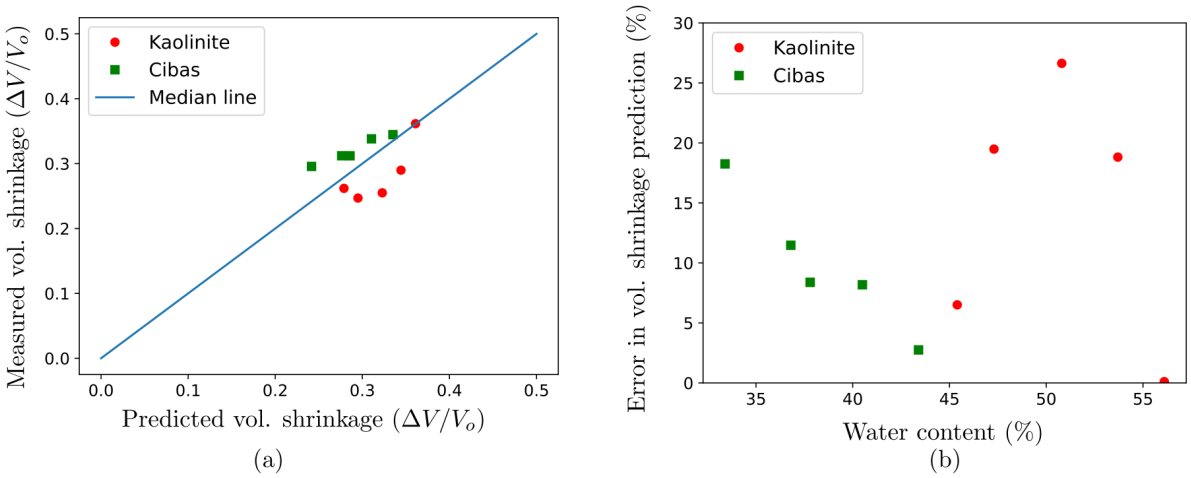

Figure 3.18: Shrinkage prediction (a) comparison of measured volumetric shrinkage with predicted volumetric shrinkage (b) Error in volumetric shrinkage prediction vs water content

there was less error in the prediction. However, for height in Cibas clay, the model seems to be over-predictive, whereas, for diameter in Kaolinite, the model seems to underestimate the size. Again the error is calculated based on the predicted and measured linear dimension which is given by the absolute difference in the predicted and measured linear dimension divided by the measured dimension. These errors are less than the errors in volumetric shrinkage prediction. The prediction error for linear dimension is less than 6% of the original observed size in Figure 3.19c. For Cibas clay, the error in height is less than 3%, and that in diameter is less than 2%. Whereas, for Kaolinite, the error in height is less than 3%, and for diameter, it changes between 3 and 6%. The error in diameter prediction for Kaolinite seems to increase and then decrease with the water content. The reason for the prediction error might be because of non-uniform drying. Moreover, the dimensions of the dried specimen are measured by Vernier Calipers to the precision of 0.01mm, whereas the models are assumed to be printed precisely to the designed size, which may not be true.

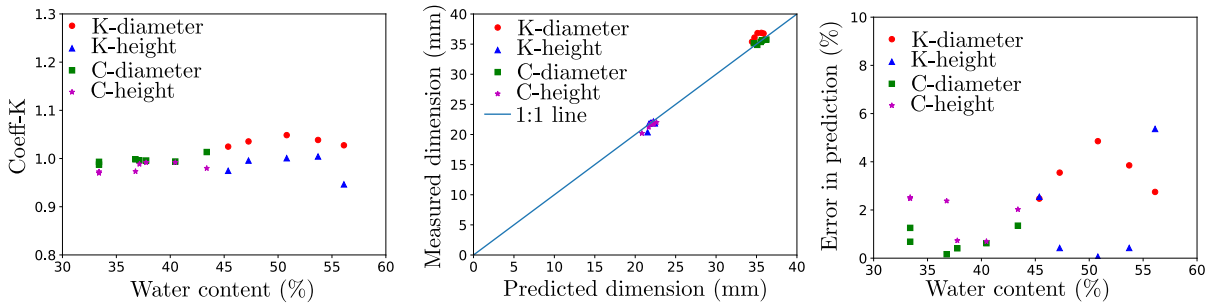

Figure 3.19: Shrinkage test results (a) variation of β with water content; (b) comparison of measured dimension with the predicted ones; and (c) variation of error in size prediction with water content (D and H in the parenthesis represent the value of shrunk diameter and shrunk height respectively for the printed specimen from the corresponding clay).

3.5 Discussion

This study proposes using Atterberg limits and liquidity index as fundamental controlling material parameters to relate 3D printing quality with operation parameters such as pneumatic pressure, nozzle diameter, travel velocity, and extrusion rate. To find the relationships between these parameters, analytical models are derived based on Bernoulli's continuity principles applied in a modular fashion to all composite components of the extrusion system of the 3D printer used for the analysis. This approach can be applied to different printing mechanisms and is a valid alternative to understanding the mechanisms that produce good-quality prints for various clays. Using the models and material characterization techniques described in this study, various objects with intricate shapes were 3D printed, as shown in Figure 3.20. As shown in the Figure, these print jobs did not require trial and error to be printed at acceptable quality. Although it is a marginal saving in desktop applications, it could save significant amounts of time and economic resources when dealing with large-scale prototypes, especially with new material from natural sources.

This study recommends a printing consistency within the 50 - 80% LI range, correlating to a pressure range between 250 kPa and 850 kPa for optimal 3D printing with

Figure 3.20: Various printed objects as an application of developed model

the WASP 40100 clay printer. The clay paste balances fluidity and solidity within this specified range, ensuring good layer adhesion, structural stability, and minimal shrinkage.

A simple procedure like the flow rate and Atterberg limit tests are recommended to characterize material and printer parameter combinations fully. However, further research is needed considering an expanded material and printer configuration database. Further research is needed to investigate rheological effects, transient flow rates arising from a depleting clay reservoir, adhesion behavior, and the effect of boundary conditions on the desiccation and shrinkage process of the clay. For instance, Chen et al. [96] found that the adhesion factor is influenced by the cohesive strength of the clay, which in turn is largely dependent on water content. However, they also stated that as long as the clay is fully

saturated, the adhesion factor for clay in this specific context should be considered constant.

The shrinkage model is developed considering no decrease in volume below SL of the clay. The specimen printed for the shrinkage test is assumed to be 50 mm in diameter and 20 mm in height. However, it is possible that the printed specimen diameter can be slightly smaller or larger (in tenths of mm) than the targeted. The height may change because of the vertical stress at the base of the specimen due to self-weight, which can result in a little settlement, thus changing the diameter and height. The shrinkage of the specimen is assumed to be uniform across all sides which may not be true because of different exposure conditions. Also, accurately calculating the volume is challenging due to the slight curvature on the outer layers, resulting from imperfect overlap during layering. Rapid drying leads to uneven moisture loss in specimens, resulting in significant cracking and distortion due to the non-uniform drying process. To optimize the drying process and minimize dimensional changes, addressing shrinkage requires careful calibration of printing parameters, including layer thickness, infill density, print speed, and moisture content. Additionally, employing techniques such as gradual drying or controlled environments can help mitigate shrinkage effects and enhance the overall quality of the printed objects [84]. The shrinkage model will be instrumental in determining the scaling factor, which helps to obtain the size of the specimen that needs to be printed to obtain the target size.

Various research avenues are still needed to explore, including the effects of water content and printing parameters on the interlayer adhesion, the effects of pozzolanic additives such as cement and lime on the printability and subsequent material strength, the development of standards and codes, and methodologies to design printing mixtures from indigenous material sources.

3.6 Conclusions

This study has demonstrated the critical role of Atterberg limits and the liquidity index in controlling the extrudability and quality of 3D-printed clay objects. The analytical 1D modular model developed in this research successfully relates the liquidity index, undrained shear strength, extrusion rate, nozzle diameter, and bid thickness with the pressure at the piston. Experimental results validate the model, highlighting the importance of the liquidity index as a key parameter in optimizing the 3D printing process of earthen materials. The following conclusions are derived from the results of this study.

1. The research highlights that the change in clay's water content significantly impacts its consistency, and strength, directly affecting the outcome of the AM process. The liquidity index (LI) is identified as the controlling state parameter that helps to fine-tune the extrudability and quality of clay 3D-printed objects. The undrained shear strength (S_u) increases exponentially with a decrease in the liquidity index (LI). As a result the pneumatic pressure increases. Based on the experiments, the study recommends maintaining the printing consistency within a LI of 50-80% for optimal printing conditions with the WASP 40100 clay 3D printer.

2. The results from the 3D printing validate the operating pressure prediction model well. The study also designed an easy and inexpensive experimental method known as flow rate tests to determine operating pressure to avoid under and over-extrusion of clay paste. Utilizing these models facilitates the swift determination of operating pressure, thereby conserving valuable time and minimizing material wastage that would otherwise occur during trial-and-error processes aimed at pressure determination.

3. The study presents a shrinkage prediction model based on the water content and Atterberg's limits. The results of the shrinkage tests on the printed specimens indicate that the shrinkage model can be used to predict post-drying shrinkage

effectively for research or practice in achieving high-precision engineering with earthen materials. The model allows for the determination of the scaling factor which helps for pre-adjustment of printing dimensions to achieve the desired final product size, addressing the critical aspect of shrinkage management in earthen 3D printing.

4. The study concludes that the developed models and material characterization techniques provide valuable insights into the application of earthen materials in 3D printing. The research positions earthen 3D printing as a viable and environmentally friendly approach in the construction sector. The models are effective in optimizing the printing process and ensuring the quality of printed objects, with potential applications in both desktop and large-scale 3D printing projects.

CHAPTER 4
CONCLUSION AND RECOMMENDATIONS

4.1 Conclusions

The study comprehensively investigates the optimization of 3D-printed clay objects by analyzing the interplay between extrusion pressure, soil moisture content, liquidity index, and the geometrical configuration of the extrusion equipment. The developed analytical models for operating pressure predictions and shrinkage predictions validated with the experimental results highlight the importance of liquidity index and Atterberg's limits in optimizing the 3D printing process of earthen materials. The conclusions of the study are as follows:

- The mathematical model for operating pressure prediction is successfully developed and validated with the experimental results. This model will save time in determining the operating pressure compared to doing trials to find optimum pressure avoiding over and under-extrusion.

- Threshold and operating pneumatic pressures are directly related to the undrained shear strength (S_u) of the clay which in turn is related to its liquidity index (LI). The pressures increase with the decrease in LI (i.e., decrease in water content) and decrease with increase in LI (i.e., increase in water content). Based on the experiments, the study recommends maintaining the printing consistency within a LI of 50-80% for optimal printing conditions with the WASP 40100 clay 3D printer.

- The pressures are sensitive to the geometrical configurations of the extrusion equipment. Based on the first mathematical model, adjusting parameters such as the L/D ratio and nozzle diameter can alter the required pressures for optimal extrusion. It underscores the significant impact of equipment geometry, where larger orifices and smaller clay column depths necessitate lower pressures.

- The research underscores the proportional relationship between moisture content and the extent of shrinkage in printed objects. The research conducted provided a model validated with experimental results that can predict post-drying shrinkage based on water content and Atterberg's limits. This model allows for the pre-adjustment of printing dimensions to achieve the desired final product size, addressing the issue of shrinkage management in earthen 3D printing.

4.2 Future work recommendations

The work presented in this thesis has laid a foundational understanding of the interplay between Atterberg limits, liquidity index, and their impacts on the 3D printing process using earthen materials. The models can predict the operating pressure and shrinkage reasonably well. However, some aspects warrant further investigation to enhance the depth and applicability of this research. The recommendations for future work are as follows:

4.2.1 Material Diversity

Future investigations should incorporate a wider array of earthen materials, including various types of clays and clay mixtures with different additives. The influence of organic and inorganic admixtures on the extrudability and post-processing behavior, such as drying shrinkage and mechanical strength, would provide a more comprehensive understanding of the material properties.

4.2.2 Variation of α

The variation of the adhesion factor with the water content should be studied and incorporated into the operating pressure prediction model.

4.2.3 Rheological Studies

An in-depth rheological study of clay mixtures before and after extrusion could offer insights into their flow behavior under different pressures and shear rates. These studies

should include the effects of viscosity on the extrusion process and the quality of 3D-printed objects.

4.2.4 Printer Configuration

Expanding the research to include various printer configurations and extrusion mechanisms would contribute to a more versatile application of the developed models. Understanding how different extruder geometries and operational parameters affect the printing process is crucial for the customization of 3D printers.

4.2.5 Sustainability Analysis

Further work is needed to quantify the sustainability benefits of using local earthen materials in 3D printing. This should include lifecycle assessment studies focusing on the carbon footprint, energy consumption, and overall environmental impact compared to traditional construction materials and methods.

4.2.6 Shrinkage Control

Additional research is warranted to refine the shrinkage prediction model. This includes investigating the impacts of different drying regimes, environmental conditions, and post-processing techniques to control and mitigate shrinkage.

4.2.7 Mechanical Property Evaluation

Future work should also involve the assessment of the mechanical properties of 3D-printed specimens under various loading conditions. Long-term durability studies under environmental loading would also be beneficial.

4.2.8 Large-Scale Printing and Field Testing

There is a pressing need to transition from laboratory-scale to full-scale printing to validate the scalability of the process. Field tests that involve printing larger structures will

help in understanding the challenges and potential of earthen material printing in real-world construction.

By pursuing these recommendations, future researchers can build upon the foundation established in this thesis, advancing the field of additive manufacturing with earthen materials and moving towards a more sustainable construction paradigm.

REFERENCES

[1] Maria Pilar Gómez Tena, Jessica Gilabert, Javier Montolio, Jorge Corrales, M. Toledo, and M. Pérez. *3D PRINTING OF CERAMIC PIECES BY EXTRUDING CLAY SUSPENSIONS*. February 2016.

[2] Chen Wang, Fayun Liang, and Xiong Yu. Experimental and numerical investigations on the performance of sacrificial piles in reducing local scour around pile groups. *Natural Hazards*, 85(3):1417–1435, February 2017.

[3] Jonathan Keep. A Guide to Clay 3D Printing. November 2020.

[4] Zeming He, T.S. Shanmugasundaram, and Gurdev Singh. Inkjet 3D printing of clay ceramics for water treatment. *Progress in Additive Manufacturing*, 3(4):215–219, June 2018. MAG ID: 2807725674 S2ID: 92be5d5b040bd91865dd5a7d22cda1be90240220.

[5] Alberto Chiusoli. La prima Casa Stampata in 3D generata con la Terra | Gaia, September 2018.

[6] Alberto Chiusoli. Casa stampata in 3D TECLA, January 2021.

[7] ASTM F2792. *Terminology for Additive Manufacturing Technologies,*. ASTM International, 2012.

[8] Erwin Peng, Danwei Zhang, and Jun Ding. Ceramic Robocasting: Recent Achievements, Potential, and Future Developments. *Advanced Materials*, 30(47):1802404, 2018. _eprint: https://onlinelibrary.wiley.com/doi/pdf/10.1002/adma.201802404.

[9] Daniel Maskell, Andrew Heath, and Pete Walker. Laboratory scale testing of extruded earth masonry units. *Materials & Design*, 45:359–364, March 2013.

[10] Amnah Y. Alqenaee, Ali M. Memari, and Maryam Hojati. TRANSITION FROM TRADITIONAL COB CONSTRUCTION TO 3D PRINTING OF CLAY HOMES. *Journal of Green Building*, 16(4):3–28, September 2021. MAG ID: 4205456404 S2ID: 09f3b347628f760d0180e0721c6fabfb189f1470.

[11] Marwah M. Thajeel and György L. Balázs. 3D printing for earth construction - review. *Concrete Structures*, 23:64–67, 2022.

[12] Elena Ferretti, Massimo Moretti, Alberto Chiusoli, Lapo Naldoni, Francesco De Fabritiis, and Massimo Visonà. Mechanical Properties of a 3D-Printed Wall Segment Made with an Earthen Mixture. *Materials*, 15(2):438, January 2022.

[13] Javier Alonso Madrid, Guillermo Sotorrío Ortega, Javier Gorostiza Carabaño, Nils O. E. Olsson, and José Antonio Tenorio Ríos. 3D Claying: 3D Printing and Recycling Clay. *Crystals*, 13(3):375, February 2023.

[14] Arnaud Perrot, Damien Rangeard, and Eric Courteille. 3D printing of earth-based materials: Processing aspects. *Construction and Building Materials*, 172:670–676, 2018. ISBN: 0950-0618 Publisher: Elsevier.

[15] Alexandre Dubor, Edouard Cabay, and Angelos Chronis. Energy efficient design for 3D printed earth architecture. In *Humanizing Digital Reality: Design Modelling Symposium Paris 2017*, pages 383–393. Springer, 2018.

[16] Flávio Craveiro, Helena Bártolo, Shadi Nazarian, Paulo Bártolo, and Jose Duarte. *Additive Manufacturing of Functionally Graded Building Parts: Towards Seamless Architecture*. March 2018.

[17] Diana Ürge Vorsatz, Nick Eyre, Peter Graham, Danny Harvey, Edgar Hertwich, Yi Jiang, Christian Kornevall, Mili Majumdar, James E. McMahon, Sevastianos Mirasgedis, Shuzo Murakami, Aleksandra Novikova, Kathryn Janda, Omar Masera, Michael McNeil, Ksenia Petrichenko, Sergio Tirado Herrero, and Eberhard Jochem. Energy End-Use: Buildings. In Global Energy Assessment Writing Team, editor, *Global Energy Assessment: Toward a Sustainable Future*, pages 649–760. Cambridge University Press, Cambridge, 2012.

[18] Hashem Alhumayani, Mohamed Gomaa, Veronica Soebarto, and Wassim Jabi. Environmental assessment of large-scale 3D printing in construction: A comparative study between cob and concrete. *Journal of Cleaner Production*, 270:122463, October 2020.

[19] Tuan D. Ngo, Alireza Kashani, Gabriele Imbalzano, Kate T.Q. Nguyen, and David Hui. Additive manufacturing (3D printing): A review of materials, methods, applications and challenges. *Composites Part B: Engineering*, 143:172–196, June 2018.

[20] Benay Gürsoy. From Control to Uncertainty in 3D Printing with Clay. pages 21–30, Łódź, Poland, 2018.

[21] C. P. Wroth and D. M. Wood. The correlation of index properties with some basic engineering properties of soils. *Canadian Geotechnical Journal*, 15(2):137–145, 1978. ISBN: 0008-3674 Publisher: NRC Research Press Ottawa, Canada.

[22] Bharat Bhushan and Matt Caspers. An overview of additive manufacturing (3D printing) for microfabrication. *Microsystem Technologies*, 23(4):1117–1124, April 2017.

[23] Susmita Bose. Bone tissue engineering using 3D printing. *Materials Today*, 16(12):496–504, December 2013. Publisher: Elsevier.

[24] S. Scott Crump. Apparatus and method for creating three-dimensional objects, June 1992.

[25] Chee Kai Chua, Kah Fai Leong, and Chu Sing Lim. *Rapid Prototyping: Principles And Applications (3rd Edition) (With Companion Cd-rom)*. World Scientific Publishing Company, January 2010. Google-Books-ID: PiI8DQAAQBAJ.

[26] Zhangwei Chen, Ziyong Li, Junjie Li, Chengbo Liu, Changshi Lao, Yuelong Fu, Changyong Liu, Li Yang, Pei Wang, Pei Wang, and He Yi. 3D printing of ceramics: A review. *Journal of The European Ceramic Society*, 39(4):661–687, April 2019. MAG ID: 2900429435.

[27] Fused Deposition of Ceramics: A New Technique for the Rapid Fabrication of Ceramic Components: Materials Technology: Vol 10, No 7-8.

[28] Mohammad Taufik and Prashant K. Jain. A Study of Build Edge Profile for Prediction of Surface Roughness in Fused Deposition Modeling. *Journal of Manufacturing Science and Engineering*, 138(061002), January 2016.

[29] Omar A. Mohamed, Syed H. Masood, and Jahar L. Bhowmik. Optimization of fused deposition modeling process parameters: a review of current research and future prospects. *Advances in Manufacturing*, 3(1):42–53, March 2015.

[30] Anoop Kumar Sood, Raj K. Ohdar, and Siba S. Mahapatra. Parametric appraisal of mechanical property of fused deposition modelling processed parts. *Materials & Design*, 31(1):287–295, 2010. Publisher: Elsevier.

[31] Jasgurpreet Singh Chohan, Rupinder Singh, Kamaljit Singh Boparai, Rosa Penna, and Fernando Fraternali. Dimensional accuracy analysis of coupled fused deposition modeling and vapour smoothing operations for biomedical applications. *Composites Part B: Engineering*, 117:138–149, 2017. Publisher: Elsevier.

[32] Pedram Parandoush and Dong Lin. A review on additive manufacturing of polymer-fiber composites. *Composite Structures*, 182:36–53, 2017. Publisher: Elsevier.

[33] Xin Wang, Man Jiang, Zuowan Zhou, Jihua Gou, and David Hui. 3D printing of polymer matrix composites: A review and prospective. *Composites Part B: Engineering*, 110:442–458, 2017. Publisher: Elsevier.

[34] Rui Dou, Tianming Wang, Yunshan Guo, and Brian Derby. Ink-Jet Printing of Zirconia: Coffee Staining and Line Stability. *Journal of the American Ceramic Society*, 94(11):3787–3792, November 2011.

[35] Hue P. Le. Progress and Trends in Ink-jet Printing Technology. *Journal of Imaging Science and Technology*, 42:49–62, January 1998. Publisher: Society of Imaging Science and Technology.

[36] Nahum Travitzky, Nahum Travitzky, Alexander Bonet, Benjamin Dermeik, Tobias Fey, Ina Filbert-Demut, Lorenz Schlier, Tobias Schlordt, and Peter Greil. Additive Manufacturing of Ceramic-Based Materials. *Advanced Engineering Materials*, 16(6):729–754, June 2014. MAG ID: 1642712619.

[37] Behrokh Khoshnevis. Automated construction by contour crafting—related robotics and information technologies. *Automation in construction*, 13(1):5–19, 2004. Publisher: Elsevier.

[38] Charles W. Hull. Apparatus for production of three-dimensional objects by stereolithography, March 1986.

[39] Zak C. Eckel, Chaoyin Zhou, John H. Martin, Alan J. Jacobsen, William B. Carter, and Tobias A. Schaedler. Additive manufacturing of polymer-derived ceramics. *Science*, 351(6268):58–62, January 2016.

[40] S. J. Leigh, C. P. Purssell, J. Bowen, D. A. Hutchins, J. A. Covington, and D. R. Billson. A miniature flow sensor fabricated by micro-stereolithography employing a magnetite/acrylic nanocomposite resin. *Sensors and Actuators A: Physical*, 168(1):66–71, July 2011.

[41] Weiwu Chen, Soshu Kirihara, and Yoshinari Miyamoto. Fabrication and Measurement of Micro Three-Dimensional Photonic Crystals of SiO2 Ceramic for Terahertz Wave Applications. *Journal of the American Ceramic Society*, 90(7):2078–2081, 2007. _eprint: https://onlinelibrary.wiley.com/doi/pdf/10.1111/j.1551-2916.2007.01676.x.

[42] Francesca Scalera, Carola Esposito Corcione, Francesco Montagna, Alessandro Sannino, and Alfonso Maffezzoli. Development and characterization of UV curable epoxy/hydroxyapatite suspensions for stereolithography applied to bone tissue engineering. *Ceramics International*, 40(10, Part A):15455–15462, December 2014.

[43] David P. Sarment, Khalaf Al-Shammari, and Christopher E. Kazor. Stereolithographic Surgical Templates for Placement of Dental Implants in Complex Cases. | International Journal of Periodontics & Restorative Dentistry | EBSCOhost, June 2003. ISSN: 0198-7569 Issue: 3 Pages: 286 Volume: 23.

[44] Ferry PW Melchels, Jan Feijen, and Dirk W. Grijpma. A review on stereolithography and its applications in biomedical engineering. *Biomaterials*, 31(24):6121–6130, 2010. Publisher: Elsevier.

[45] Jill Z. Manapat, Qiyi Chen, Piaoran Ye, and Rigoberto C. Advincula. 3D Printing of Polymer Nanocomposites via Stereolithography. *Macromolecular Materials and Engineering*, 302(9):1600553, September 2017.

[46] Ben Utela, Duane Storti, Rhonda Anderson, and Mark Ganter. A review of process development steps for new material systems in three dimensional printing (3DP). *Journal of Manufacturing Processes*, 10(2):96–104, 2008. Publisher: Elsevier.

[47] Hyub Lee, Chin Huat Joel Lim, Mun Ji Low, Nicholas Tham, Vadakke Matham Murukeshan, and Young-Jin Kim. Lasers in additive manufacturing: A review. *International Journal of Precision Engineering and Manufacturing-Green Technology*, 4(3):307–322, July 2017.

[48] Ian Gibson Ian Gibson. Additive manufacturing technologies 3D printing, rapid prototyping, and direct digital manufacturing, 2015.

[49] F. Wang, J. Mei, H. Jiang, and X. Wu. Laser fabrication of Ti6Al4V/TiC composites using simultaneous powder and wire feed. *Materials Science and Engineering: A*, 445-446:461–466, February 2007.

[50] Slic3r - Open source 3D printing toolbox.

[51] A. Ruscitti, C. Tapia, and N. M. Rendtorff. A review on additive manufacturing of ceramic materials based on extrusion processes of clay pastes. *Cerâmica*, 66(380):354–366, December 2020.

[52] A. Moropoulou, A. Bakolas, and S. Anagnostopoulou. Composite materials in ancient structures. *Cement and Concrete Composites*, 27(2):295–300, February 2005.

[53] Mohamed Abdelkader, Stanislav Petrik, Daisy Nestler, and Mateusz Fijalkowski. Ceramics 3D Printing: A Comprehensive Overview and Applications, with Brief Insights into Industry and Market. *Ceramics*, 7(1):68–85, March 2024. Number: 1 Publisher: Multidisciplinary Digital Publishing Institute.

[54] Jen Owen. 3D Printed Ceramics | Introducing 3D Potter Printers, June 2023.

[55] J.J. Simonis and A.K. Basson. Manufacturing a low-cost ceramic water filter and filter system for the elimination of common pathogenic bacteria. *Physics and Chemistry of the Earth, Parts A/B/C*, 50-52:269–276, 2012.

[56] D. van Halem, H. van der Laan, S. G. J. Heijman, J. C. van Dijk, and G. L. Amy. Assessing the sustainability of the silver-impregnated ceramic pot filter for low-cost household drinking water treatment. *Physics and Chemistry of the Earth, Parts A/B/C*, 34(1):36–42, January 2009.

[57] H. M. Murphy, M. Sampson, E. McBean, and K. Farahbakhsh. Influence of household practices on the performance of clay pot water filters in rural Cambodia. *Desalination*, 248(1):562–569, November 2009.

[58] Mariette Moevus, Yves Jorand, Christian Olagnon, Sandrine Maximilien, Romain Anger, Laetitia Fontaine, and Laurent Arnaud. Earthen construction: an increase of the mechanical strength by optimizing the dispersion of the binder phase. *Materials and Structures*, 49(4):1555–1568, April 2016.

[59] Sadek Deboucha and Roslan Hashim. A review on bricks and stabilized compressed earth blocks. *Sci. Res. Essays*, February 2011.

[60] Laurence Keefe. *Earth Building: Methods and Materials, Repair and Conservation*. Routledge, 0 edition, May 2012.

[61] D. Gallipoli, A. W. Bruno, and C. Perlot & N. Salmon. Raw earth construction: Is there a role for unsaturated soil mechanics? In *Unsaturated Soils: Research & Applications*. CRC Press, 2014. Num Pages: 8.

[62] Horst Schroeder. *Sustainable Building with Earth*. Springer International Publishing, Cham, 2016.

[63] Douglas Readle, Sarah Coghlan, Jonathan C. Smith, Andrew Corbin, and Charles E. Augarde. Fibre reinforcement in earthen construction materials. *Proceedings of the Institution of Civil Engineers - Construction Materials*, 169(5):252–260, October 2016. Publisher: ICE Publishing.

[64] Johann Plank. Applications of biopolymers and other biotechnological products in building materials. *Applied Microbiology and Biotechnology*, 66(1):1–9, November 2004.

[65] Leandro Dario Serraiocco, Diego Barbero, Andrea Maroni, and Sandra Peyrot. Effects of lime-stabilization of A-4 Soils in its Monotonic Strength and Deformation parameters for Road Use. *Journal of Geotechnical Engineering*, March 2021.

[66] Diego Barbero, Leandro Dario Serraiocco, Andrea Maroni, and Sandra Peyrot. Portland Cement for A-4 Group Soils Stabilization. *Journal of Geotechnical Engineering*, March 2021.

[67] M. Moretti, A. Chiusoli, L. Naldoni, F. De Fabritiis, and M. Visonà. Earthen 3d printed constructions towards a new high-efficient way of building. *Past and Present of the Earthen Architectures in China and Italy; Luvidi, L., Fratini, F., Rescic, S., Zhang, J., Eds*, pages 147–155, 2021.

[68] Elena Ferretti, Moretti Massimo, Alberto Chiusoli, Lapo Naldoni, Francesco De Fabritiis, and Massimo Visonà. Rice-Husk Shredding as a Means of Increasing the Long-Term Mechanical Properties of Earthen Mixtures for 3D Printing, 2022.

[69] S. Muguda, G. Lucas, P. N. Hughes, C. E. Augarde, C. Perlot, A. W. Bruno, and D. Gallipoli. Durability and hygroscopic behaviour of biopolymer stabilised earthen construction materials. *Construction and Building Materials*, 259:119725, October 2020.

[70] Tiziano Li Piani, Dennis Krabbenborg, Jaap Weerheijm, Lambertus Koene, and Lambertus J. Sluijs. THE MECHANICAL PERFORMANCE OF TRADITIONAL ADOBE MASONRY COMPONENTS: AN EXPERIMENTAL-ANALYTICAL CHARACTERIZATION OF SOIL BRICKS AND MUD MORTAR. *Journal of Green Building*, 13(3):17–44, June 2018.

[71] Erwan Hamard, Bogdan Cazacliu, Andry Razakamanantsoa, and Jean-Claude Morel. Cob, a vernacular earth construction process in the context of modern sustainable building. *Building and Environment*, 106:103–119, September 2016.

[72] Amnah Y. Alqenaee, Ali M. Memari, and Maryam Hojati. TRANSITION FROM TRADITIONAL COB CONSTRUCTION TO 3D PRINTING OF CLAY HOMES. *Journal of Green Building*, 16(4):3–28, September 2021.

[73] P. Guilherme, M. J. Ribeiro, and J. A. Labrincha. Behaviour of different industrial ceramic pastes in extrusion process. *Advances in Applied Ceramics*, 108(6):347–351, August 2009.

[74] Miki Takahashi, Kazuo Mizoguchi, Keigo Kitamura, and Koji Masuda. Effects of clay content on the frictional strength and fluid transport property of faults. *Journal of Geophysical Research: Solid Earth*, 112(B8), 2007. ISBN: 0148-0227 Publisher: Wiley Online Library.

[75] Jony. Clay for 3D printing, January 2021.

[76] Paul Calvert and Robert Crockett. Chemical Solid Free-Form Fabrication: Making Shapes without Molds. *Chemistry of Materials*, 9(3):650–663, March 1997. Publisher: American Chemical Society.

[77] Sihan Wang, Hui Ping Toh, Felix Raspall, and Carlos Banon. Detailing the Configuration to Perform Better Clay Printing. pages 153–161, Bangkok, Thailand, 2020.

[78] Abdullah Ibrahim. shrinkage in clay 3D printing, April 2017.

[79] Karim Touati, Malo Le Guern, Yassine El Mendili, Athmane Azil, François Streiff, Jim Carfrae, Matthew Fox, Steve Goodhew, and Mohamed Boutouil. Earthen-based building: *In-situ* drying kinetics and shrinkage. *Construction and Building Materials*, 369:130544, March 2023.

[80] John Benbow and John Bridgwater. Paste flow and extrusion. 1993. Publisher: Clarendon Press Oxford.

[81] Fernando A. Andrade, Hazim A. Al-Qureshi, and Dachamir Hotza. Modeling of clay paste extrusion through a rectangular die. *International Review of Chemical Engineering*, 2(4):478–483, 2010. ISBN: 2035-1755 Publisher: Praise Worthy Prize, FEDERICO II University 21 Claudio Naples I 80125 Italy.

[82] H. Tajiri, E. Pieri, and H. Al-Qureshi. Modified modeling of clay paste extrusion through a circular die: Beyond the Steady-State. *Int J Metall Metal Phys*, 4:1–9, 2019.

[83] Arnaud Perrot, Christophe Lanos, Yannick Melinge, and Patrice Estellé. Mortar physical properties evolution in extrusion flow. *Rheologica Acta*, 46(8):1065–1073, September 2007.

[84] Fuwen Hu, Tadeusz Mikolajczyk, Danil Yurievich Pimenov, and Munish Kumar Gupta. Extrusion-based 3D printing of ceramic pastes: Mathematical modeling and in situ shaping retention approach. *Materials*, 14(5):1137, 2021. ISBN: 1996-1944 Publisher: MDPI.

[85] M. J. Ribeiro, J. M. Ferreira, and J. A. Labrincha. Plastic behaviour of different ceramic pastes processed by extrusion. *Ceramics International*, 31(4):515–519, 2005. ISBN: 0272-8842 Publisher: Elsevier.

[86] Arthur Casagrande. Classification and identification of soils. *Transactions of the American Society of Civil Engineers*, 113(1):901–930, 1948. ISBN: 0066-0604 Publisher: American Society of Civil Engineers.

[87] Philotheos Lokkas, Ioannis Chouliaras, Theodoros Chrisanidis, Dimitrios Christodoulou, Emmanouil Papadimitriou, and Evangelos Paschalis. Historical background and evolution of Soil Mechanics. *WSEAS TRANSACTIONS ON ADVANCES in ENGINEERING EDUCATION*, 18:96–113, August 2021.

[88] Casagrande A. Research on the Atterberg limits of soils. *Public Roads*, 13(8):121–136, 1932.

[89] ASTM D4318. *Standard Test Methods for Liquid Limit, Plastic Limit, and Plasticity Index of Soils*. ASTM International, 2017.

[90] Binu Sharma and Padma K. Bora. Plastic Limit, Liquid Limit and Undrained Shear Strength of Soil—Reappraisal. 2003.

[91] I. Littleton. An experimental study of the adhesion between clay and steel. *Journal of Terramechanics*, 13(3):141–152, October 1976.

[92] ASTM D4943. *Standard Test Method for Shrinkage Factors of Cohesive Soils by the Water Submersion Method*. ASTM International, 2018.

[93] ASTM D7928. *Test Method for Particle-Size Distribution (Gradation) of Fine-Grained Soils Using the Sedimentation (Hydrometer) Analysis*. ASTM International, 2021.

[94] Shaharyar Ahmad, Muzaffar Ali, Furqan Ali, Shahzeb Ahmad, Daniyal Ahmad, and Obaid Iftikhar. Design and Experimental Investigation of Thermosiphoning Heat Transfer through Nanofluids in Compound Parabolic Collector. *Engineering Proceedings*, 12:39, January 2022.

[95] Ji XianJun, Liang Ying, Cao WenHao, Sun XiaoKang, and Song Peng. Determination of Static and Dynamic Yield Stress of Chengdu Clay Slurry. *Frontiers in Physics*, 10, August 2022. Publisher: Frontiers.

[96] Xiuhan Chen, J Broecke, G Liu, Guojun Hong, and Sape Miedema. *A STUDY ON THE CLAY ADHESION FACTOR*. June 2019.

APPENDICES

APPENDIX A

PRINTING TIME MEASUREMENT USING AN ACCELEROMETER SENSOR

Figure A.1: Witmotion accelerometer attached to the extruder to measure printing time

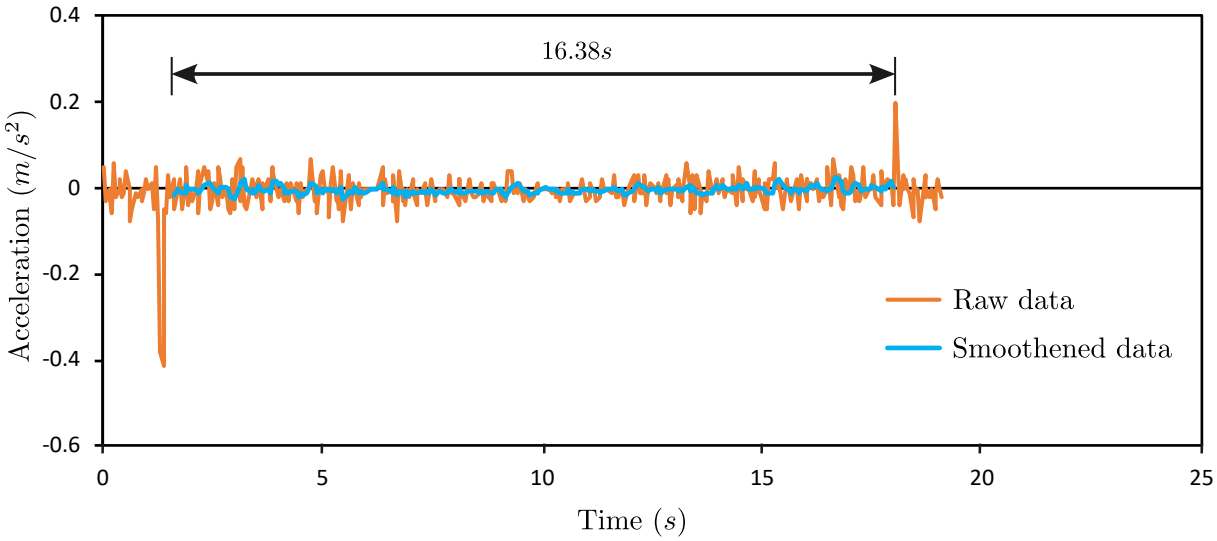

Figure A.2: Print time measurement for a bid 250 mm long, 2 mm wide, and 1mm high for flow rate test

APPENDIX B

EXPERIMENTAL RESULTS FROM EXTRUSION TESTS, 3D PRINTING TESTS, FLOW RATE TESTS AND SHRINKAGE TESTS

B.1 Extrusion test

Table B.1: Extrusion test results

S.N.	**Kaolinite**			**Cibas clay**			**Presumpscot clay**		
	w (%)	**LI (%)**	P_{nt} **(kPa)**	**w (%)**	**LI (%)**	P_{nt}**(kPa)**	**w (%)**	**LI (%)**	P_{nt} **(kPa)**
1	57.5	98.1	43	44.5	102.2	20	51.7	102.5	32
2	55.3	89.6	40	44.3	101.3	20	50.9	99.5	39
3	54.3	86.0	50	44.1	100.4	21	50.4	97.8	34
4	54.1	85.0	55	43.9	99.4	25	48.9	92.3	42
5	53.9	84.2	65	43.8	99.1	23	48.0	88.8	38
6	53.8	83.8	60	43.4	97.5	35	47.9	88.5	41
7	53.4	82.3	62	43.3	96.9	35	47.2	86.0	44
8	53.1	81.0	65	43.0	95.6	30	46.1	81.9	47
9	52.7	79.6	61	42.7	94.5	32	45.1	78.1	46
10	52.1	77.5	60	42.4	93.3	45	44.7	76.7	42
11	52.1	77.3	43	42.3	92.4	35	43.7	73.1	43
12	51.8	76.0	69	42.1	91.6	40	43.7	73.1	43
13	51.6	75.2	50	42.1	91.5	45	43.7	73.0	53
14	51.3	74.2	45	41.5	89.2	40	43.5	72.3	46
15	51.0	73.0	78	41.5	89.1	50	43.5	72.3	46
16	50.6	71.5	51	41.4	88.9	45	42.9	70.0	55
17	50.4	70.8	60	41.3	88.2	50	42.5	68.3	55
18	50.3	70.3	67	41.0	86.8	50	42.3	67.8	44
19	49.7	67.9	56	40.9	86.7	46	41.9	66.3	56
20	49.7	67.9	75	40.9	86.7	52	41.8	65.9	42
21	49.4	67.1	62	40.8	86.3	49	41.3	64.1	66

Continued on next page

Table B.1 Continued from previous page

S.N.	Kaolinite			Cibas clay			Presumpscot clay		
22	49.4	66.9	62	40.7	85.7	42	40.9	62.5	60
23	49.3	66.4	49	40.4	84.3	45	40.7	61.8	60
24	49.2	66.3	73	40.3	84.1	45	40.1	59.6	57
25	49.1	65.7	67	39.8	81.6	55	40.0	59.1	65
26	48.8	64.4	78	39.6	80.9	55	39.7	58.2	70
27	48.1	62.0	77	39.0	78.3	50	39.6	57.9	70
28	47.7	60.4	65	38.7	77.0	48	39.5	57.5	75
29	47.7	60.3	65	37.6	72.1	60	39.4	57.2	57
30	47.5	59.6	66	37.4	71.3	50	39.4	57.2	70
31	47.5	59.6	66	37.4	71.3	60	39.3	56.6	80
32	47.3	58.7	81	36.7	68.3	70	38.8	55.0	85
33	46.8	56.9	102	35.7	63.9	85	38.7	54.3	61
34	46.6	56.0	72	35.5	62.9	64	38.5	53.7	70
35	46.3	55.1	73	35.1	61.3	95	38.4	53.4	90
36	46.3	55.0	68	34.8	60.2	66	38.3	53.0	95
37	46.2	54.6	114	34.4	58.3	89	38.0	51.7	95
38	46.1	54.3	89	34.4	58.2	86	37.7	50.7	100
39	45.7	52.6	115	33.9	56.2	69	37.0	48.1	105
40	45.2	50.8	122	33.6	54.8	100	36.4	46.0	115
41	44.4	47.8	127	33.3	53.4	72	36.3	45.6	125
42	44.4	47.5	136	33.2	53.0	110	36.2	45.1	135
43	43.8	45.5	140	32.7	51.0	78	35.4	42.1	140
44	43.6	44.4	156	32.1	48.3	130	35.1	40.9	88
45	43.3	43.6	142	31.9	47.3	92	34.9	40.5	160
46	42.8	41.5	166	31.4	45.2	130	34.6	39.3	180
47	41.6	36.9	150	31.1	43.7	106	34.4	38.6	102
48	41.6	36.9	155	30.6	41.7	127	33.8	36.3	195
49	41.3	35.8	162	29.4	36.7	134	33.5	35.0	93
50	40.3	31.8	173	29.1	35.2	149	32.7	32.2	211

Continued on next page

Table B.1 Continued from previous page

S.N.	Kaolinite			Cibas clay			Presumpscot clay		
51	40.2	31.5	178	28.6	33.0	153	30.2	22.9	189

B.2 3D printing tests

Table B.2: Printing pressures for Kaolinite with water content and LI: total pressure (P_t), piston resistance (P_r) and pneumatic operation pressure (P_{no})

w (%)	LI (%)	P_t (kPa)	P_r (kPa)	P_{no} (kPa)
45.8	53.0	605.0	40.0	565.0
56.2	93.1	260.0	59.4	200.6
53.7	83.6	322.0	40.0	282.0
52.8	79.8	400.0	40.0	360.0
52.4	78.3	380.0	35.6	344.4
51.2	73.9	357.0	34.2	322.8
50.8	72.3	480.0	86.5	393.6
49.9	68.8	348.0	47.2	300.8
49.8	68.5	492.0	43.3	448.7
49.6	67.5	480.0	52.0	428.0
49.5	67.3	486.0	40.0	446.0
49.5	67.2	536.0	40.0	496.0
49.3	66.5	503.0	45.4	457.6
48.1	62.0	670.0	58.0	612.0
47.9	61.3	348.0	33.0	315.0
47.3	58.7	654.0	68.0	586.0
45.4	51.4	672.3	33.6	638.7

Table B.3: Printing pressures for Cibas clay with water content and LI: total pressure (P_t), piston resistance (P_r) and net pressure (P_{no})

w (%)	LI (%)	P_t (kPa)	P_r (kPa)	P_{no} (kPa)
43.7	98.9	210.0	49.2	160.8
42.1	91.9	145.0	35.2	109.8
40.8	86.1	180.0	31.2	148.8
40.5	84.6	257.0	38.2	218.8
40.4	84.3	180.0	34.5	145.5
40.1	83.0	140.0	40.0	100.0
38.6	76.5	270.0	40.0	230.0
38.4	75.7	300.0	40.0	260.0
38.4	75.6	232.0	38.0	194.0
37.2	70.4	462.0	37.5	424.5
37.1	70.0	306.0	37.5	268.5
36.7	68.3	390.0	52.0	338.0
36.4	67.0	430.0	59.0	371.0
36.3	66.7	450.0	41.0	409.0
36.2	66.1	290.0	40.0	250.0
35.9	64.8	350.0	32.0	318.0
35.6	63.3	385.0	36.0	349.0
34.6	59.1	550.0	40.0	510.0

Table B.4: Printing pressures for Presumpscot clay with water content and LI: total pressure (P_t), piston resistance (P_r) and net pressure (P_{no})

w (%)	LI (%)	P_t (kPa)	P_r (kPa)	P_{no} (kPa)
43.7	90.6	210.0	40.0	170.0
43.1	87.9	133.0	29.2	103.8
42.1	83.9	145.0	38.3	106.8
40.5	76.9	257.0	32.3	224.7
38.4	68.3	242.0	36.9	205.1
37.2	63.3	462.0	57.2	404.8
36.3	59.8	450.0	48.3	401.7
35.6	56.7	430.0	37.4	392.6
35.6	56.5	395.0	41.5	353.6

B.3 Flow rate test results

Table B.5: Flow rate test results for Kaolinite at $LI = 61\%$

Clay type:	Kaolinite
Test No:	1
w:	47.9 %
LI:	61 %
Density of soil:	1.73 gm/cm^3

Cont. Wt. (g)	Cont. + Clay (g)	Pressure (kPa)	Time (s)	flow (g/s)	flow (mm^3/s)
1.04	1.9	670.18	16.38	0.053	30.41
0.99	1.8	649.91	16.38	0.049	28.64
0.98	1.75	624.89	16.38	0.047	27.22
0.99	1.71	600.01	16.38	0.044	25.46
1.01	1.53	550.45	16.38	0.032	18.38
1.03	1.27	499.36	16.38	0.015	8.49

Table B.6: Flow rate test results for Kaolinite at $LI = 69\%$

Clay type:	Kaolinite
Test No:	2
w:	50.0 %
LI:	69 %
Density of soil:	1.71 gm/cm^3

Cont. Wt. (g)	Cont. + Clay (g)	Pressure (kPa)	Time (s)	flow (g/s)	flow (mm^3/s)
1.00	2.04	600.89	16.38	0.063	37.13
1.03	1.99	550.26	16.38	0.059	34.27
0.98	1.83	500.36	16.38	0.052	30.35
0.96	1.68	449.76	16.38	0.044	25.70
0.99	1.4	400.89	16.38	0.025	14.64
1.03	1.24	300.12	16.38	0.013	7.50

Table B.7: Flow rate test results for Kaolinite at $LI = 94\%$

Clay type:	Kaolinite
Test No:	3
w:	56.4 %
LI:	94 %
Density of soil:	1.66 gm/cm^3

Cont. Wt. (g)	Cont. + Clay (g)	Pressure (kPa)	Time (s)	flow (g/s)	flow (mm^3/s)
0.97	2.15	500.24	16.38	0.072	43.35
0.97	2.08	449.61	16.38	0.068	40.78
1.08	2.05	401.36	16.38	0.059	35.64
1.03	1.83	325.73	17.38	0.046	27.70
1.03	1.7	300.17	16.38	0.041	24.62
1.03	1.48	275.02	18.38	0.024	14.73

Table B.8: Flow rate test results for Kaolinite at $LI = 106\%$

Clay type:	Kaolinite
Test No:	4
w:	59.4 %
LI:	106 %
Density of soil:	1.64 gm/cm^3

Cont. Wt. (g)	Cont. + Clay (g)	Pressure (kPa)	Time (s)	flow (g/s)	flow (mm^3/s)
1.02	2.29	450.38	17.38	0.073	44.54
1.03	2.2	401.26	16.38	0.071	43.54
0.99	2.1	375.67	16.38	0.068	41.30
1.02	2.05	350.7	16.38	0.063	38.33
0.98	1.96	300.12	16.38	0.060	36.47
0.99	1.63	250.73	16.38	0.039	23.81

Table B.9: Flow rate test results for Cibas Clay at $LI = 59\%$

Clay type:	Cibas
Test No:	1
w:	34.6 %
LI:	59 %
Density of soil:	1.86 gm/cm^3

Cont. Wt. (g)	Cont. + Clay (g)	Pressure (kPa)	Time (s)	flow (g/s)	flow (mm^3/s)
1.05	2.35	671.05	16.38	0.079	42.64
1.01	2.19	599.87	16.38	0.072	38.70
1.01	2.08	550.61	16.38	0.065	35.10
1.05	1.99	500.23	16.38	0.057	30.83
1.02	1.78	449.25	17.38	0.044	23.49
1.00	1.51	400.36	18.38	0.028	14.91

Table B.10: Flow rate test results for Cibas Clay at $LI = 70\%$

Clay type:	Cibas
Test No:	2
w:	37.1 %
LI:	70 %
Density of soil:	1.83 gm/cm^3

Cont. Wt. (g)	Cont. + Clay (g)	Pressure (kPa)	Time (s)	flow (g/s)	flow (mm^3/s)
1.00	2.41	500.17	16.38	0.086	46.95
0.99	2.36	451.26	16.38	0.084	45.62
1.06	2.23	400.16	16.38	0.071	38.96
1.03	2.13	349.28	16.38	0.067	36.63
1.03	1.94	300.89	17.38	0.052	28.56
1.02	1.56	249.39	18.38	0.029	16.02

Table B.11: Flow rate test results for Cibas Clay at $LI = 81\%$

Clay type:	Cibas
Test No:	3
w:	39.6 %
LI:	81 %
Density of soil:	1.81 gm/cm^3

Cont. Wt. (g)	Cont. + Clay (g)	Pressure (kPa)	Time (s)	flow (g/s)	flow (mm^3/s)
1.03	1.49	180.34	16.38	0.028	15.56
1.01	1.51	201.02	16.38	0.031	17.17
1.07	2.11	250.40	16.38	0.063	34.90
1.05	2.30	301.80	16.38	0.076	42.10
0.99	2.37	351.44	16.38	0.084	46.53
1.00	2.53	401.77	17.38	0.088	48.75

Table B.12: Flow rate test results for Cibas Clay at $LI = 89\%$

Clay type:	Cibas
Test No:	4
w:	41.5 %
LI:	89 %
Density of soil:	1.79 gm/cm^3

Cont. Wt. (g)	Cont. + Clay (g)	Pressure (kPa)	Time (s)	flow (g/s)	flow (mm^3/s)
0.99	1.30	125.04	16.38	0.019	10.60
1.00	2.02	149.84	16.38	0.062	34.72
1.01	2.42	199.32	16.38	0.086	48.16
1.01	2.50	200.76	16.38	0.091	50.96

Table B.13: Flow rate test results for Presumpscot Clay at $LI = 58\%$

Clay type:	Presumpscot
Test No:	1
w:	36.0 %
LI:	58 %
Density of soil:	1.84 gm/cm^3

Cont. Wt. (g)	Cont. + Clay (g)	Pressure (kPa)	Time (s)	flow (g/s)	flow (mm^3/s)
1.05	2.3	551.04	16.38	0.076	41.38
0.99	2.14	499.86	16.38	0.070	37.96
0.99	2.05	449.97	16.38	0.065	35.25
0.99	1.86	400.77	16.38	0.053	28.74
1.02	1.44	350.67	16.38	0.026	14.10
1.01	1.16	300.87	16.38	0.009	4.88

Table B.14: Flow rate test results for Presumpscot Clay at $LI = 69\%$

Clay type:	Presumpscot
Test No:	2
w:	38.6 %
LI:	69 %
Density of soil:	1.82 gm/cm^3

Cont. Wt. (g)	Cont. + Clay (g)	Pressure (kPa)	Time (s)	flow (g/s)	flow (mm^3/s)
0.98	2.75	451.29	16.38	0.108	59.47
1.03	2.45	400.64	16.38	0.087	47.91
1.06	2.3	350.05	16.38	0.076	41.85
1.01	2.24	301.24	16.38	0.075	41.30
1.01	1.86	251.06	16.38	0.052	28.63
1.01	1.26	200.25	16.38	0.015	8.40

Table B.15: Flow rate test results for Presumpscot Clay at $LI = 81\%$

Clay type:	Presumpscot
Test No:	3
w:	41.5 %
LI:	81 %
Density of soil:	1.79 gm/cm^3

Cont. Wt. (g)	Cont. + Clay (g)	Pressure (kPa)	Time (s)	flow (g/s)	flow (mm^3/s)
1.04	10.49	500	60	0.158	88.17
0.98	8.65	400	60	0.128	71.66
1.02	9.64	300	90	0.096	53.74
1.02	6.47	200	120	0.045	25.19
1.02	4.42	100	100	0.034	19.03

Table B.16: Flow rate test results for Presumpscot Clay at $LI = 84\%$

Clay type:	Presumpscot
Test No:	4
w:	42.1 %
LI:	84 %
Density of soil:	1.78 gm/cm^3

Cont. Wt. (g)	Cont. + Clay (g)	Pressure (kPa)	Time (s)	flow (g/s)	flow (mm^3/s)
1.01	2.64	275	16.38	0.100	55.92
1.02	2.52	250	16.38	0.092	51.46
1.08	2.35	200	16.38	0.078	43.57
1.1	1.94	140	16.38	0.051	28.82

Table B.17: Flow rate test results for Presumpscot Clay at $LI = 88\%$

Clay type:	Presumpscot
Test No:	5
w:	43.1 %
LI:	88 %
Density of soil:	1.77 gm/cm^3

Cont. Wt. (g)	Cont. + Clay (g)	Pressure (kPa)	Time (s)	flow (g/s)	flow (mm^3/s)
0.99	1.2	75.19	16.38	0.013	7.24
1.01	2.43	200.38	16.38	0.087	48.97
1.02	2.31	174.61	16.38	0.079	44.49
0.99	2.12	148.38	16.38	0.069	38.97
1.04	1.82	125.29	16.38	0.048	26.90
0.99	1.61	100.87	16.38	0.038	21.38

B.4 Shrinkage tests

B.4.1 Tests to calibrate shrinkage model

The following data are common for each clay for the determination of shrinkage.

Total volume of the container : 84.30 cm^3

Raw volume of printed specimen : 39.27 cm^3

Mass of container : 14.04 g

Mass of container + water : 98.34 g

Density of wax : 0.92 g/cm^3

Table B.18: Shrinkage test results for Cibas clay by Water Submersion Method

w (%)	Dry specimen mass (g)	Dry mass + wax (g)	dry mass + wax +container + water (g)	wax mass (g)	water mass (g)	volume of wax (cm^3)	Volume of dry specimen (cm^3)	Volumetric Shrinkage (%)
56.2	38.29	39.17	110.96	0.88	57.75	0.96	25.59	34.83
52.8	50.17	50.57	121.72	0.40	57.11	0.43	26.76	31.87
52.4	39.69	41.05	111.53	1.36	56.44	1.48	26.38	32.82
49.8	42.63	43.95	114.35	1.32	56.36	1.43	26.51	32.51
49.3	40.89	41.84	112.92	0.95	57.04	1.03	26.23	33.21
48.1	43.26	44.44	113.22	1.18	54.74	1.28	28.28	27.99
47.9	41.88	43.19	114.05	1.31	56.82	1.42	26.06	33.65
45.8	45.12	46.04	115.85	0.92	55.77	1.00	27.53	29.90

Table B.19: Shrinkage test results for Cibas clay by Water Submersion Method

w (%)	Dry specimen mass (g)	Dry mass + wax (g)	dry mass + wax +container + water (g)	wax mass (g)	water mass (g)	volume of wax (cm^3)	Volume of dry specimen (cm^3)	Volumetric Shrinkage (%)
43.5	48.67	49.07	120.78	0.40	57.67	0.43	26.20	33.29
40.1	51.10	53.14	122.36	2.04	55.18	2.22	26.90	31.49
39.9	51.86	52.78	122.46	0.92	55.64	1.00	27.66	29.56
38.7	55.63	56.65	126.08	1.02	55.39	1.11	27.80	29.20
38.5	49.20	50.43	119.28	1.23	54.81	1.34	28.15	28.31
38.4	52.47	53.64	124.54	1.17	56.86	1.27	26.17	33.36
38.4	49.77	50.90	120.04	1.13	55.10	1.23	27.97	28.77
37.2	47.35	48.07	117.82	0.72	55.71	0.78	27.81	29.19
36.4	51.89	52.56	121.85	0.67	55.25	0.73	28.32	27.88
36.2	50.01	50.44	121.79	0.43	57.31	0.47	26.52	32.46
34.6	51.34	51.85	122.81	0.51	56.92	0.55	26.83	31.69

Table B.20: Shrinkage test results for Presumpscot clay by Water Submersion Method

w (%)	Dry specimen mass (g)	Dry mass + wax (g)	dry mass + wax +container + water (g)	wax mass (g)	water mass (g)	volume of wax (cm^3)	Volume of dry specimen (cm^3)	Volumetric Shrinkage (%)
42.1	50.06	50.45	122.65	0.39	58.16	0.42	25.72	34.51
40.5	46.97	48.33	118.68	1.36	56.31	1.48	26.51	32.49
38.4	49.41	49.86	121.30	0.45	57.40	0.49	26.41	32.75
37.2	53.47	54.90	124.03	1.43	55.09	1.55	27.66	29.58
36.3	47.58	49.33	117.82	1.75	54.45	1.90	27.95	28.83
35.6	51.33	51.76	121.49	0.43	55.69	0.47	28.14	28.34

B.4.2 Shrinkage tests to evaluate shrinkage model

Table B.21: Shrinkage prediction and measurement for Kaolinite

Specimen size (dia. × ht.) mm	w (%)	Linear shrinkage	Predicted dia. (mm)	Predicted ht. (mm)	Measured dia. (mm)	Measured ht. (mm)	% error	% error
40 × 25	56.1	0.86	34.45	21.53	35.40	20.38	2.37	4.62
40 × 25	53.7	0.87	34.75	21.72	36.09	21.81	3.35	0.37
40 × 25	50.8	0.88	35.12	21.95	36.83	21.97	4.26	0.05
40 × 25	47.3	0.89	35.61	22.25	36.87	22.16	3.16	0.38
40 × 25	45.4	0.90	35.87	22.42	36.76	21.85	2.22	2.28
63 × 24	56.1	0.86	54.26	20.67	55.94	19.44	2.67	5.12
63 × 24	53.7	0.87	54.73	20.85	56.70	20.98	3.13	0.53

Table B.22: Shrinkage prediction and measurement for Cibas

Specimen size (dia. × ht.) mm	w (%)	Linear shrinkage	Predicted dia. (mm)	Predicted ht. (mm)	Measured dia. (mm)	Measured ht. (mm)	% error	% error
40 × 25	43.4	0.87	34.67	21.67	35.14	21.23	1.17	1.75
40 × 25	40.5	0.88	35.09	21.93	34.88	21.76	0.55	0.70
40 × 25	37.8	0.89	35.51	22.19	35.36	22.01	0.36	0.73
40 × 25	36.8	0.89	35.67	22.29	35.61	21.70	0.15	2.38
40 × 25	33.4	0.91	36.22	22.64	35.77	22.02	1.14	2.47
63 × 23	33.4	0.91	57.05	20.83	56.66	20.20	0.62	2.52
63 × 26	37.1	0.89	56.08	23.14	55.87	22.88	0.33	1.03
42 × 16	37.1	0.89	37.39	14.24	37.28	13.88	0.26	2.27

B.5 Undrained shear strength test results

Table B.23: Undrained shear strength with water content and LI for Kaolinite, Cibas and Presumpscot clay

Kaolinite			Cibas			Presumpscot		
w (%)	LI (%)	Su (kPa)	w (%)	LI (%)	Su (kPa)	w (%)	LI (%)	Su (kPa)
54.3	86.0	3.1	44.3	101.3	2.1	51.7	123.6	1.5
53.8	83.8	3.2	43.9	99.4	2.3	50.9	120.3	1.6
52.1	77.5	3.6	43.0	95.6	2.5	50.4	118.3	1.5
51.8	76.0	8.5	42.7	94.5	2.5	48.9	112.2	1.8
51.6	75.2	4	42.3	92.4	2.7	48.0	108.2	2.1
51.3	74.2	3.7	42.1	91.6	2.1	47.9	107.9	1.8
51.0	73.0	8.6	41.5	89.2	3.1	47.2	105.0	2.0
50.9	72.7	3.9	41.4	88.9	2.2	46.1	100.2	2.8
50.6	71.5	4.2	40.9	86.7	2.3	45.1	96.3	3.1
50.4	70.8	8.8	40.8	86.3	2.5	44.7	94.5	3.5
50.3	70.3	5	40.7	85.7	3.4	43.7	90.6	1.4
49.9	68.8	10	40.4	84.3	2.6	43.7	90.5	3.2
49.7	67.9	4.7	40.3	84.1	3.6	43.5	89.6	1.8
49.5	67.3	4.6	39.3	79.5	2.8	42.9	87.1	3.6
49.4	67.1	5	39.0	78.3	3.7	42.5	85.2	2.3
49.3	66.4	4.9	38.7	77.0	3.7	42.3	84.6	1.9
49.2	66.3	5.6	38.6	76.3	3.3	41.9	83.0	4.3
49.1	65.7	6.1	37.8	73.1	3.4	41.8	82.4	2.6
48.8	64.4	6.1	37.4	71.3	3.7	41.3	80.4	4.2
48.4	63.3	7.1	37.2	70.3	3.8	40.7	77.7	4.4
48.2	62.4	6.3	35.5	62.9	6.3	40.1	75.3	4
48.1	62.0	12	34.8	60.2	6.3	39.4	72.7	4.3
47.7	60.3	7.4	34.4	58.2	7.1	38.7	69.4	7.6
47.5	59.6	7.6	33.9	56.2	7.6	38.5	68.7	4.2
47.3	58.7	7.9	33.3	53.4	10	38.0	66.8	4.9
46.8	56.9	15	32.7	51.0	13	35.1	54.4	8.2
46.6	56.0	8.3	31.9	47.3	15	34.4	51.8	10
46.3	55.1	9.1	31.1	43.7	16	33.5	47.8	11
46.3	55.0	8.7	30.6	41.7	18			
46.2	54.7	17	29.4	36.7	21			
46.1	54.3	16						
45.7	52.6	18						
45.2	50.6	21						
44.4	47.8	21						
44.4	47.5	25						
43.6	44.4	26						
43.3	43.6	24						
42.8	41.5	33						
41.6	36.9	28						
40.3	31.8	47						

APPENDIX C

DETAILED DERIVATION OF THE MATHEMATICAL MODELS USED IN THE STUDY

C.1 Threshold pressure to initiate clay paste extrusion

Applying the equilibrium condition of forces on the differential element in Figure 3.3, Equation C.1 is obtained.

$$\sigma_z A_z = \left(\sigma_z + \frac{d\sigma_z}{dz}dz\right) A_z + F_L \tag{C.1}$$

where, $F_L = \alpha S_u dz \pi D_z$ and $A_z = \dfrac{\pi D_z^2}{4}$ is cross-sectional area of the clay paste flow; D_z is the diameter of the strip which is $D_z = D$ for section $z = 0$ to $z = L$ and $D_z = d + 2(L + l - z)\tan\theta$ for the section $z = L$ to $z = L + l$. Rearranging Equation C.1, Equation C.2 is obtained.

$$\left(-\frac{d\sigma_z}{dz}dz\right)\frac{\pi D_z^2}{4} = \alpha S_u dz \pi D_z \tag{C.2}$$

Simplifying Equation C.2, we obtained Equation C.3.

$$-\frac{d\sigma_z}{dz} = \frac{4\alpha S_u}{D_z} \tag{C.3}$$

To obtain an expression for pressure inside the tank with distance, equation C.3 is integrated from $z = 0$ to $z = L + l$ where extrusion pressure is equal to σ_p at $z = 0$ and 0 at $z = L + l$ resulting in Equation C.4.

$$\int_{\sigma_p}^{0} -d\sigma_z = \int_0^{L+l} \frac{4\alpha S_u}{D_z}\, dz = \int_0^{L} \frac{4\alpha S_u}{D}\, dz + \int_L^{L+l} \frac{4S_u}{d + 2(L + l - z)\tan\theta}\, dz \tag{C.4}$$

The first part of integral C.4 is integrated to obtain equation C.1.

$$\int_0^{L} \frac{4\alpha S_u}{D}\, dz = \frac{4\alpha S_u L}{D} \tag{C.5}$$

The second integral can be solved by substituting $u = d + 2(l - z)\tan\theta$, which gives $du = -2\tan\theta\, dz$ to obtain Equation C.6

$$\int_{L}^{L+l} \frac{4\alpha S_u}{d + 2(l - z)\tan\theta}\, dz = -\frac{2S_u}{\tan\theta} \int_{d+2l\tan\theta}^{d} \frac{1}{u}\, du \tag{C.6}$$

This integral evaluates to

$$-\frac{2S_u}{\tan\theta} \left[\ln|u|\right]_{d+2l\tan\theta}^{d} = -\frac{2S_u}{\tan\theta} \left[\ln|d| - \ln|d + 2l\tan\theta|\right]$$

Therefore, the total integral is given by Equation C.7:

$$\sigma_p = \frac{4\alpha S_u L}{D} - \frac{2S_u}{\tan\theta} \left[\ln|d| - \ln|d + 2l\tan\theta|\right]$$

$$\sigma_p = \frac{4\alpha S_u L}{D} - \frac{2S_u}{\tan\theta} \ln\left(\frac{d}{d + 2l\tan\theta}\right) \tag{C.7}$$

Equation C.7 represents the pneumatic on the piston to extrude the clay. It does not include the piston resistance. The undrained shear strength of the clay can be related to its LI by the Equation C.8 proposed by Wroth and Wood [21].

$$S_u = 1.7 P_a exp(-4.6LI) \tag{C.8}$$

where, P_a is the atmospheric pressure. Now, substituting S_u from Equation C.8 and $\theta = 45^\circ$ which also results in $d + 2l = D$ in Equation C.7, Equation C.9 is obtained.

$$\sigma_p = 3.4 P_a \left[2\alpha \left(\frac{L}{D}\right) - \ln\left(\frac{d}{D}\right)\right] exp(-4.6LI) \tag{C.9}$$

Adding piston friction resistance P_r to the above equation, the threshold extrusion pressure is obtained as described in Equation C.10.

$$P_t = P_r + 3.4 P_a \left[2\alpha \left(\frac{L}{D}\right) - \ln\left(\frac{d}{D}\right)\right] exp(-4.6LI) \tag{C.10}$$

C.2 Extrusion pressure model for pneumatic piston coupled with screw

The extrusion velocity v_e relating to bid width w_b and thickness t_b is given by equation C.11.

$$v_e = \frac{4 w_b t_b V_t}{\pi {d_n}^2} \tag{C.11}$$

where V_t is the travel velocity of the nozzle. Equation C.11 shows that for constant extrusion velocity, the print layer decreases proportionally to the increase of travel velocity and vice-versa.

To derive the expression for the pressure on the piston in the tank, the equation of continuity and Bernoulli's equation are applied between different levels in Figure 3.5. Applying Bernoulli's equation and continuity equation between levels 3 and 4 (nozzle), Equation C.12 is obtained.

$$z_3 + \frac{P_3}{\gamma_s} + \frac{v_3^2}{2g} - h_{l3} = \frac{P_4}{\gamma_s} + \frac{v_4^2}{2g} \tag{C.12}$$

where, γ_s is unit weight of clay paste, d_f is diameter of feeder tube, and h_{f3} is friction loss in screw. At the nozzle $P_4 = P_a = 0$ (atmospheric pressure) and $v_4 = v_e$ (extrusion velocity)

Applying the continuity equation between the nozzle and level 3:
$v_3 = \left(\frac{d_n}{d_f}\right)^2 v_e$

Total energy loss in screw:

$$(h_{l3}) = h_{f3} + h_{c3} = \frac{\alpha S_u (2 D_s W_s + 2 H_s (D_s - H_s - W_s))}{(D_s H_s - H_s^2)\gamma_s} + \frac{K_3}{2g}\left(\frac{d_n^2}{d_{n1}^2} - 1\right)^2 v_e^2$$

Now, Equation C.12 is simplified as Equation C.13.

$$P_3 = \gamma_s \left(\frac{v_e^2}{2g} + h_{f3} - z_3 - \frac{\left(\frac{d_n}{d_f}\right)^4 v_e^2}{2g} \right) \tag{C.13}$$

Applying Bernoulli's equation between 2 and 3, Equation C.14 is obtained.

$$z_2 + \frac{P_2}{\gamma_s} + \frac{v_2^2}{2g} - h_{f2} = \frac{P_3}{\gamma_s} + \frac{v_3^2}{2g} \tag{C.14}$$

From continuity equation, $V_2 = V_3$ (level 2 and 3 have same diameters, $d_2 = d_f$

Friction loss in the feeder tube:

$$h_{f2} = \frac{4\alpha S_u l_f}{\gamma_s d_f}$$

where l_f is the length of the feeder tube.

Now, Equation C.14 can be simplified to Equation C.15.

$$P_2 = \gamma_s \left(\frac{P_3}{\gamma_s} + \frac{4\alpha S_u l_f}{\gamma_s d_f} - z_2 \right) \tag{C.15}$$

Applying Bernoulli's equation between 1 and 2, Equation C.16 is obtained.

$$z_1 + \frac{P_1}{\gamma_s} + \frac{v_1^2}{2g} - h_{f1} - h_{c1} = \frac{P_2}{\gamma_s} + \frac{v_2^2}{2g} \tag{C.16}$$

Applying continuity equation between 1 and nozzle:

$$v_1 = \left(\frac{d_n}{D}\right)^2 v_e$$

Applying continuity equation between 2 and nozzle:

$$v_3 = v_2 = \left(\frac{d_n}{d_f}\right)^2 v_e$$

Now, Equation C.16 can be simplified to Equation C.17.

$$z_1 + \frac{P_1}{\gamma_s} + \frac{v_1^2}{2g} - \left[\frac{4\alpha S_u(z-l)}{D\gamma_s} + \frac{4S_u l}{\left(\frac{D+d_f}{2}\right)\gamma_s}\right] - \frac{K_1(v_1-v_2)^2}{2g} = \frac{P_2}{\gamma_s} + \frac{v_2^2}{2g} \tag{C.17}$$

where, D is the diameter of the clay tank and K_1 is contraction coefficient at level 2. Equation C.17 is solved in the following steps shown below to obtain the final Equation C.18

$$z_1 + \frac{P_1}{\gamma_s} + \frac{v_1^2 - v_2^2}{2g} - \frac{K_1(v_1-v_2)^2}{2g} - \frac{4S_u}{\gamma_s}\left[\frac{\alpha(z_1-l)}{D} + \frac{2l}{(D+d_f)}\right] = \frac{P_2}{\gamma_s}$$

$$z_1 + \frac{P_1}{\gamma_s} + \frac{v_e^2}{2g}d_n^4\left(\frac{1}{D^4} - \frac{1}{d_f^4}\right) - \frac{K_1 v_e^2}{2g}d_n^4\left(\frac{1}{D^2} - \frac{1}{d_f^2}\right)^2 - \frac{4S_u}{\gamma_s}\left[\frac{\alpha(z_1-l)}{D} + \frac{2l}{(D+d_f)}\right] = \frac{P_2}{\gamma_s}$$

$$P_1 = \gamma_s\left[\frac{P_2}{\gamma_s} - z_1 - \frac{v_e^2}{2g}d_n^4\left(\frac{1}{D^4} - \frac{1}{d_f^4}\right) + \frac{K_1 v_e^2}{2g}d_n^4\left(\frac{1}{D^2} - \frac{1}{d_f^2}\right)^2 + \frac{4S_u}{\gamma_s}\left[\frac{\alpha(z_1-l)}{D} + \frac{2l}{(D+d_f)}\right]\right] \tag{C.18}$$

where, D is the diameter of the clay tank and K is contraction coefficient at level 2. Equation C.18 connects the optimum extrusion pressure required to print clay paste to the depth of the clay in the tank $(L+l)$, tank diameter (D), feeder tube diameter (d_f), nozzle diameter (d_n) and extrusion velocity (V_n) which is connected to the print layer thickness (t_b), width (w_b) and nozzle travel velocity (V_t). The pressure estimates obtained from this equation are plotted in Figure 3.12 and compared with the experimental results.

C.3 Energy loss in the extruder

Total energy loss $h_{l3} = h_{f3} + h_{c3}$ where h_{f3} is friction loss in screw and h_{c3} is contraction loss in nozzle.

Friction loss in screw (h_{f3})

$$h_{f3} = \frac{\text{friction force between surface of screw and clay paste}}{\text{soil unit weight per unit length}}$$

$$h_{f3} = \frac{\alpha\pi(D_s - 2H_s)W_s S_u + \alpha\pi D_s W_s S_u + 2\alpha\pi H_s S_u(D_s - H_s)}{\frac{\pi}{4}(D_s^2 - (D_s - 2H_s)^2)\gamma_s}$$

$$h_{f3} = \frac{\alpha\pi S_u((D_s - 2H_s)W_s + D_s W_s + 2H_s(D_s - H_s))}{\frac{\pi}{4}(4D_s H_s - 4H_s^2)\gamma_s}$$

$$h_{f3} = \frac{\alpha S_u(2D_s W_s + 2H_s(D_s - H_s - W_s))}{(D_s H_s - H_s^2)\gamma_s}$$

Contraction loss in nozzle (h_{c3})

Applying the continuity equation between the nozzle base and nozzle tip,

$$v_{e1} = \left(\frac{d_n}{d_{n1}}\right)^2 v_e$$

where, d_{n1} and v_{e1} are the diameter and flow velocity at the nozzle base; d_n and v_e are diameter and extrusion velocity at nozzle tip

$$h_{c3} = K_3\frac{(v_{e1} - v_e)^2}{2g} = \frac{K_3}{2g}\left(\frac{d_n^2}{d_{n1}^2} - 1\right)^2 v_e^2$$

where, K_3 is the contraction coefficient at level 4.

Total loss (h_{l3}) $= h_{f3} + h_{c3} = \frac{\alpha S_u(2D_s W_s + 2H_s(D_s - H_s - W_s))}{(D_s H_s - H_s^2)\gamma_s} + \frac{K_3}{2g}\left(\frac{d_n^2}{d_{n1}^2} - 1\right)^2 v_e^2$

BIOGRAPHY OF THE AUTHOR

Rakesh Kumar Pandit was born on September 20, 1996, in the southern region of Nepal. Following the completion of his primary and middle school education in his hometown in 2013, he ventured to Kathmandu, the capital of Nepal, to pursue his high school studies. In 2015, he successfully graduated from high school at Nepal Mega College and gained admission to the Institute of Engineering, Pulchowk Campus, Tribhuvan University, where he earned a Bachelor of Engineering in Civil Engineering in 2021. After gaining valuable experience by working for a year at the Civil Work Consultancy in Kathmandu, Rakesh decided to further his education. Consequently, he enrolled in the University of Maine in the fall of 2022 to pursue his M.Sc. in Civil Engineering.

Rakesh Kumar Pandit is a candidate for the Master of Science degree in Civil Engineering from the University of Maine in May 2024.